

# Dynamic migration of rotating neutron stars due to a phase transition instability

Harald Dimmelmeier<sup>1\*</sup>, Michal Bejger<sup>2†</sup>, Pawel Haensel<sup>2‡</sup> and J. Leszek Zdunik<sup>2§</sup>

<sup>1</sup>*Department of Physics, Aristotle University of Thessaloniki, GR-54124 Thessaloniki, Greece*

<sup>2</sup>*Copernicus Astronomical Center, Polish Academy of Sciences, Bartycka 18, 00-716 Warszawa, Poland*

Accepted <date>. Received <date>; in original form <date>

## ABSTRACT

Using numerical simulations based on solving the general relativistic hydrodynamic equations with the CoCoNuT code, we study the dynamics of a phase transition in the dense core of isolated rotating neutron stars, triggered by the back bending instability reached via angular momentum loss. In particular, we investigate the dynamics of a migration from an unstable configuration into a stable one, which leads to a mini-collapse of the neutron star and excites sizeable pulsations in its bulk until it acquires a new stable equilibrium state. We consider two equations of state which exhibit softening at high densities, a simple analytic one with a mixed hadron-quark phase (where the hadron pressure is approximated by a polytrope) in an intermediate pressure interval and pure quark matter at very high densities, and a microphysical one that has a first-order phase transition at constant pressure with a jump in density, originating from kaon condensation. Although the marginally stable initial models are rigidly rotating, we observe that during the collapse (albeit little) differential rotation is created. We analyze the emission of gravitational radiation in such an event, which in some models is amplified by mode resonance effects, and assess its prospective detectability by current and future interferometric detectors. We expect that the most favorable conditions for dynamic migration exist in very young magnetars. The rate of such events in our Galaxy is of the order of one per century and rises to about one per year if the Virgo cluster of galaxies is considered. We find that the damping of the post-migration pulsations and, accordingly, of the gravitational wave signal amplitude strongly depends on the character of the equation of state softening (either via a density jump or continuous through a mixed state). The damping of pulsations in the models with the microphysical equation of state is caused by dissipation associated with matter flowing through the density jump at the edge of the dense core. If at work, this mechanism dominates over all other types of dissipation, like bulk viscosity in the exotic-phase core, gravitational radiation damping, or numerical viscosity.

**Key words:** hydrodynamics – relativity – methods: numerical – stars: neutron – stars: pulsations – stars: phase-transition – stars: rotation

## 1 INTRODUCTION

One of the mysteries of neutron stars is the structure of their cores where the density exceeds normal nuclear density  $\rho_{\text{nuc}} \approx 3 \times 10^{14} \text{ g cm}^{-3}$ . For  $\rho \lesssim \rho_{\text{nuc}}$  the constituents of dense matter are well known (neutrons, protons, and electrons). Here the respective physical theories can be confronted with nuclear physics data and are therefore under

control (see e.g. Haensel, Potekhin & Yakovlev 2007). However, for  $\rho$  significantly larger than  $\rho_{\text{nuc}}$ , the predictions of different plausible theories diverge with increasing density. The structure of matter at  $5 - 10 \rho_{\text{nuc}}$ , i.e. at densities characteristic for the center of massive neutron stars, is unknown. Still, in order to construct neutron star models, the equation of state (EoS) of matter in this regime is needed as an input. Some theories of dense matter predict a strong softening of the EoS at  $\rho \gtrsim 2 \rho_{\text{nuc}}$ , caused by the appearance of various exotic phases of matter, such as pion condensate, kaon condensate, or deconfined quark matter (for a review see Haensel, Potekhin & Yakovlev 2007; Glendenning 2000; Weber 1999). The prediction of observable signatures of the

\* E-mail: harrydee@mpa-garching.mpg.de

† E-mail: bejger@camk.edu.pl

‡ E-mail: haensel@camk.edu.pl

§ E-mail: jlz@camk.edu.pl

presence of exotic phases in the dense core of neutron stars is thus crucial for testing physical theories of hadronic matter at extreme densities.

A softening of the EoS is expected to influence the rotational properties of neutron stars. Today, we know some 1800 radio pulsars (i.e. rotating magnetized neutron stars), which are spinning down due to angular momentum loss via radiation. They are observed using radio telescopes, where the evolution of the rotation period with time is measured, and some of them are also being monitored by the newly constructed gravitational wave detectors (albeit without a reliable detection so far in that case). If the EoS of matter in a pulsar core actually softens at some density threshold, this could have a dramatic impact on the structure of the neutron star that completely alters the pulsar timing properties: One of the possibilities is that the pulsar could enter a back bending episode, which is reflected by the reversal of the spin-down into a spin-up (Glendenning, Pei & Weber 1997; Zdunik et al. 2006). If the softening of the EoS is sufficiently strong, the back bending could lead to an instability at which the rotating neutron star dynamically migrates to a new stable equilibrium state (Zdunik et al. 2006).

Depending on the mass of the neutron star, this migration process can be accompanied by a considerable increase in central compactness and spin-up. Immediately after migration, the spinning neutron star's bulk is expected to pulsate with sizeable amplitude, which would result in a burst of gravitational radiation. This prospect gives additional motivation for studying the dynamical migration phenomenon. A scenario with similar dynamics (i.e. a dynamic migration of rotating neutron stars towards a new stable equilibrium state at higher central density along with a spin-up, the excitation of strong pulsations, and the emission of gravitational waves) was recently investigated by Lin et al. (2006) and Abdikamalov et al. (2009). However, while in that work the original, unperturbed initial configuration is in stable equilibrium and the transient is initiated by an instantaneous change in the EoS (resulting in a somewhat artificial depletion of pressure at high densities), the migration process due to back bending need not be initiated by an ad-hoc modification of the EoS, as this instability starts at an unstable equilibrium state.

In this work we investigate the dynamics of such a migration of pulsar models, triggered by the instability described above. This is accomplished by performing fully nonlinear time-dependent numerical simulations with a two-dimensional version of the general relativistic hydrodynamics code CoCoNuT. From a multitude of existing EoSs we select two types which feature softening at high densities: The first is the simple analytic MUn EoS of Zdunik et al. (2006) which obeys a polytropic relation at low densities, describes a mixed hadron-quark phase at intermediate densities (where the hadron pressure is again approximated by a polytrope, however with a different adiabatic exponent), and has pure quark matter at very high densities. The second one is a tabulated microphysical EoS that exhibits a first-order phase transition at constant pressure with a jump in density, originating from kaon condensation. For these two EoSs, as initial models we select marginally stable rotating configurations with different baryon masses, and follow the migration and the subsequent ring-down phase for many dynamic time scales. We analyze the post-migration pulsations in terms

of amplitude, spectrum and possible damping mechanisms. Furthermore, we calculate the associated gravitational wave emission and discuss the prospects for a possible detection by current and future interferometric detectors like LIGO, VIRGO or Advanced LIGO.

This article is organized as follows: In Section 2 we present the mathematical framework and numerical setup for the simulations, while in Section 3 we give details about the two EoSs employed and introduce the marginally stable models that undergo migration. Section 4 contains a survey of the results, with a general description of the migration dynamics, an analysis of the pulsations excited by this process, information about the final equilibrium states, followed by a discussion of our models' gravitational wave emission and the detectability prospects. In Section 5 we summarize our findings and close with some conclusions. We also add some information about non-equilibrium effects in the EoSs in Appendix A and explain the damping mechanism for pulsations in models with the microphysical EoS in Appendix B.

Unless otherwise noted, we choose dimensionless units for all physical quantities by setting the speed of light and the gravitational constant to one,  $c = G = 1$ . Latin indices run from 1 to 3, Greek indices from 1 to 4.

## 2 FORMULATION AND NUMERICAL METHODS

We construct the initial equilibrium models of rotating neutron stars using a variant of the self-consistent field method described in Komatsu, Eriguchi & Hachisu (1989a) (KEH hereafter), as implemented in the code RNS (Stergioulas & Friedman 1995). This code solves the general relativistic hydrostationary equations for rotating matter distributions whose pressure obeys a barotropic EoS. The resulting equilibrium models are taken as initial data for the evolution code.

The time dependent numerical simulations are performed with the code CoCoNuT developed by Dimmelmeier, Font & Müller (2002a,b) with a metric solver based on spectral methods as described in Dimmelmeier et al. (2005). The code solves the general relativistic field equations for a curved spacetime in the  $3 + 1$  split under the assumption of the conformal flatness condition (CFC) for the three-metric. The hydrodynamics equations are formulated in conservation form, and are evolved by high-resolution shock-capturing schemes.

In the following, we present the mathematical formulation of the metric and hydrodynamics equations, and then summarize the numerical methods used for solving them. Note that this part is practically identical to Section 2 in Abdikamalov et al. (2009).

### 2.1 Metric equations

We adopt the ADM  $3 + 1$  formalism by Arnowitt, Deser & Misner (1962) to foliate a spacetime endowed with a metric  $g_{\mu\nu}$  into a set of non-intersecting spacelike hypersurfaces. The line element then reads

$$ds^2 = g_{\mu\nu} dx^\mu dx^\nu = -\alpha^2 dt^2 + \gamma_{ij}(dx^i + \beta^i dt)(dx^j + \beta^j dt), \quad (1)$$

where  $\alpha$  is the lapse function,  $\beta^i$  is the spacelike shift three-vector, and  $\gamma_{ij}$  is the spatial three-metric.

In the 3+1 formalism, the Einstein equations are split into evolution equations for the three-metric  $\gamma_{ij}$  and the extrinsic curvature  $K_{ij}$ , and constraint equations (the Hamiltonian and momentum constraints) which must be fulfilled at every spacelike hypersurface.

The fluid is specified by the rest-mass density  $\rho$ , the four-velocity  $u^\mu$ , and the pressure  $P$ , with the specific enthalpy defined as  $h = 1 + \epsilon + P/\rho$ , where  $\epsilon$  is the specific internal energy. The three-velocity of the fluid as measured by an Eulerian observer is given by  $v^i = u^i/(\alpha u^0) + \beta^i/\alpha$ , and the Lorentz factor  $W = \alpha u^0$  satisfies the relation  $W = 1/\sqrt{1 - v_i v^i}$ .

Based on the ideas of Isenberg (2008) and Wilson, Mathews & Marronetti (1996), and as it was done in the work of Dimmelmeier, Font & Müller (2002a,b), we approximate the general metric  $g_{\mu\nu}$  by replacing the spatial three-metric  $\gamma_{ij}$  with the conformally flat three-metric

$$\gamma_{ij} = \phi^4 \hat{\gamma}_{ij}, \quad (2)$$

where  $\hat{\gamma}_{ij}$  is the flat metric and  $\phi$  is a conformal factor. In this CFC approximation, the ADM equations for the spacetime metric reduce to a set of five coupled elliptic non-linear equations for the metric components,

$$\begin{aligned} \hat{\Delta}\phi &= -2\pi\phi^5 (\rho h W^2 - P) - \phi^5 \frac{K_{ij} K^{ij}}{8}, \\ \hat{\Delta}(\alpha\phi) &= 2\pi\alpha\phi^5 (\rho h(3W^2 - 2) + 5P) + \alpha\phi^5 \frac{7K_{ij} K^{ij}}{8}, \\ \hat{\Delta}\beta^i &= 16\pi\alpha\phi^4 \rho h W^2 v^i + 2\phi^{10} K^{ij} \hat{\nabla}_j (\alpha\phi^{-6}) - \frac{1}{3} \hat{\nabla}^i \hat{\nabla}_k \beta^k, \end{aligned} \quad (3)$$

where the maximal slicing condition,  $K^i_i = 0$ , is imposed. Here  $\hat{\nabla}_i$  and  $\hat{\Delta}$  are the flat space Nabla and Laplace operators, respectively. For the extrinsic curvature we have the expression

$$K_{ij} = \frac{1}{2\alpha} \left( \nabla_i \beta_j + \nabla_j \beta_i - \frac{2}{3} \gamma_{ij} \nabla_k \beta^k \right), \quad (4)$$

which closes the system (3).

We rewrite the above metric equations in a mathematically equivalent form by introducing an auxiliary vector field  $W^i$  and obtain (Saijo 2004)

$$\begin{aligned} \hat{\Delta}\phi &= -2\pi\phi^5 (\rho h W^2 - P) - \phi^{-7} \frac{\hat{K}_{ij} \hat{K}^{ij}}{8}, \\ \hat{\Delta}(\alpha\phi) &= 2\pi\alpha\phi^5 (\rho h(3W^2 - 2) + 5P) + \alpha\phi^{-7} \frac{7\hat{K}_{ij} \hat{K}^{ij}}{8}, \\ \hat{\Delta}\beta^i &= 2\hat{\nabla}_j \left( 2\alpha\phi^{-6} \hat{K}^{ij} \right) - \frac{1}{3} \hat{\nabla}^i \hat{\nabla}_k \beta^k, \\ \hat{\Delta}W^i &= 8\pi\phi^{10} \rho h W^2 v^i - \frac{1}{3} \hat{\nabla}^i \hat{\nabla}_k W^k, \end{aligned} \quad (5)$$

where the flat space extrinsic curvature is given by

$$\hat{K}_{ij} = \hat{\nabla}_i W_j + \hat{\nabla}_j W_i - \frac{2}{3} \hat{\gamma}_{ij} \hat{\nabla}_k W^k \quad (6)$$

and relates to the regular extrinsic curvature as  $\hat{K}_{ij} = \phi^2 K_{ij}$  and  $\hat{K}^{ij} = \phi^{10} K^{ij}$ . The virtue of this reformulation of the metric equations is discussed in detail by Codero-Carrión et al. (2009).

Note that the metric equations do not contain explicit time derivatives, and thus the metric is calculated by a fully constrained approach, at the cost of neglecting some evolutionary degrees of freedom in the spacetime metric (e.g. dynamical gravitational wave degrees of freedom).

The accuracy of the CFC approximation has been tested in various works, both in the context of stellar core collapse and for equilibrium models of neutron stars (for a detailed comparison between the CFC approximation and full general relativity, see Dimmelmeier et al. 2006; Ott et al. 2007, and references therein). The spacetime of rapidly (uniformly or differentially) rotating neutron star models is still very well approximated by the CFC metric (2). The accuracy of the approximation is expected to degrade only in extreme cases, such as a rapidly rotating black hole or compact binary systems.

## 2.2 General relativistic hydrodynamics

The hydrodynamic evolution of a relativistic perfect fluid is determined by a system of local conservation equations, which read

$$\nabla_\mu J^\mu = 0, \quad \nabla_\mu T^{\mu\nu} = 0, \quad (7)$$

where  $J^\mu = \rho u^\mu$  is the rest-mass current, and  $\nabla_\mu$  denotes the covariant derivative with respect to the four-metric  $g_{\mu\nu}$ . Following Banyuls et al. (1997) we introduce a set of conserved variables in terms of the primitive (physical) variables  $(\rho, v_i, \epsilon)$ :

$$D = \rho W, \quad S_i = \rho h W^2 v_i, \quad \tau = \rho h W^2 - P - D. \quad (8)$$

Using the above variables, the local conservation laws (7) can be written as a first-order, flux-conservative hyperbolic system of equations,

$$\frac{\partial \sqrt{\gamma} \mathbf{U}}{\partial t} + \frac{\partial \sqrt{-g} \mathbf{F}^i}{\partial x^i} = \sqrt{-g} \mathbf{S}, \quad (9)$$

with the state vector, flux vector, and source vector

$$\begin{aligned} \mathbf{U} &= [D, S_j, \tau], \\ \mathbf{F}^i &= [D \hat{v}^i, S_j \hat{v}^i + \delta_j^i P, \tau \hat{v}^i + P v^i], \\ \mathbf{S} &= \left[ 0, \frac{1}{2} T^{\mu\nu} \frac{\partial g_{\mu\nu}}{\partial x^j}, T^{00} \left( K_{ij} \beta^i \beta^j - \beta^j \frac{\partial \alpha}{\partial x^j} \right) + \right. \\ &\quad \left. T^{0j} \left( 2K_{ij} \beta^i - \frac{\partial \alpha}{\partial x^j} \right) + T^{ij} K_{ij} \right], \end{aligned} \quad (10)$$

respectively. Here  $\hat{v}^i = v^i - \beta^i/\alpha$ , and  $\sqrt{-g} = \alpha\sqrt{\gamma}$ , with  $g = \det(g_{\mu\nu})$  and  $\gamma = \det(\gamma_{ij})$ .

The system of hydrodynamics equations (9) is closed by an EoS, which relates the pressure to some thermodynamically independent quantities, in our case  $P = P(\rho, \epsilon)$ .

## 2.3 Numerical methods for solving the metric and hydrodynamics equations

The hydrodynamic solver performs the numerical time integration of the system of conservation equations (9) using a high-resolution shock-capturing (HRSC) scheme on a finite-difference grid. In (upwind) HRSC methods a Riemann problem has to be solved at each cell interface, which requires the reconstruction of the primitive variables  $(\rho, v^i, \epsilon)$

at these interfaces. We use the piecewise parabolic method (PPM) method for the reconstruction, which yields third-order accuracy in space for smooth flows and away from extrema. The numerical fluxes are computed by means of Marquina's approximate flux formula (Donat et al. 1998). The time update of the conserved vector  $\mathbf{U}$  is done using the method of lines in combination with a Runge–Kutta scheme with second-order accuracy in time. Once the state vector is updated in time, the primitive variables are recovered through an iterative Newton–Raphson method. To numerically solve the elliptic CFC metric equations (3) we make use of an iterative non-linear solver based on spectral methods. The combination of HRSC methods for the hydrodynamics and spectral methods for the metric equations in a multidimensional numerical code has been in detail in Dimmelmeier et al. (2005).

The CoCoNuT code utilizes Eulerian spherical polar coordinates  $\{r, \theta\}$ , as for the models discussed in this work we assume axisymmetry with respect to the rotation axis and additionally equatorial symmetry. The finite-difference grid consists of 160 radial and 40 angular grid points, which are equidistantly spaced. A small part of the grid, which initially corresponds to 20 radial grid points, covers an artificial low-density atmosphere extending beyond the stellar surface, whose rest-mass density is  $10^{-17}$  of the initial central rest-mass density of the star.

Since the calculation of the spacetime metric is computationally expensive, the metric is updated only once every 25 hydrodynamic time steps during the evolution and extrapolated when needed. The suitability of this procedure is tested and discussed in detail in Dimmelmeier, Font & Müller (2002a). We also note that tests with different grid resolutions were performed to ascertain that the regular grid resolution specified above is appropriate for our simulations.

## 2.4 Gravitational waves

The gravitational waves emitted by the collapsing neutron star are computed using the Newtonian quadrupole formula in its first time-integrated form (the first-moment of momentum density formulation as described in detail in Dimmelmeier, Font & Müller 2002b) in the variant of Shibata & Sekiguchi (2004). It yields the quadrupole wave amplitude  $A_{20}^{E2}$  as the lowest order term in a multipole expansion of the radiation field into pure-spin tensor harmonics (Thorne 1980). The wave amplitude is related to the dimensionless gravitational wave strain  $h$  in the equatorial plane (Dimmelmeier, Font & Müller 2002b)

$$h = \frac{1}{8} \sqrt{\frac{15}{\pi}} \frac{A_{20}^{E2}}{r} = 8.8524 \times 10^{-21} \frac{A_{20}^{E2}}{10^3 \text{ cm}} \frac{10 \text{ kpc}}{r}, \quad (11)$$

with  $r$  being the distance to the emitting source.

We point out that although the quadrupole formula is not gauge invariant and is only strictly valid in the Newtonian slow-motion limit, for gravitational waves emitted by pulsations of rotating neutron stars it yields results that agree very well in phase and to about 10%–20% in amplitude with more sophisticated methods (Shibata & Sekiguchi 2003; Nagar et al. 2007).

## 3 MODEL SETUP

### 3.1 Equations of state

One of our two sets of models is based on a simple analytic three-phase EoS which is identical to the mixed unstable (MUn) EoS discussed in Zdunik et al. (2006)<sup>1</sup>:

- In the normal hadronic phase, i.e. for  $\rho < \rho_1 = 3.32 \times 10^{14} \text{ g cm}^{-3}$  (corresponding to  $n_1 = 0.2 \times 10^{39} \text{ cm}^{-3}$ ), the EoS is given by a polytrope,

$$P = K \rho^\gamma, \quad (12)$$

with  $\gamma = \gamma_h = 2.5$  and a polytropic constant  $K = K_h = 1.0506 \times 10^{-2}$  (in cgs units, which equals 0.025 in units of  $\hat{\rho} c^2 / \hat{n}^{\gamma_h}$  with  $\hat{\rho} = 1.66 \times 10^{14} \text{ g cm}^{-3}$  and  $\hat{n} = 0.1 \times 10^{39} \text{ cm}^{-3}$ , see Zdunik et al. 2006). The internal energy is calculated according to the ideal gas EoS as

$$\epsilon = \frac{P}{\rho(\gamma - 1)}. \quad (13)$$

- In the mixed phase, i.e. for  $\rho_1 \leq \rho < \rho_2 = 10.79 \times 10^{14} \text{ g cm}^{-3}$  (corresponding to  $n_2 = 0.65 \times 10^{39} \text{ cm}^{-3}$ ), the EoS is again a polytrope, now with  $\gamma = \gamma_m = 1.3$  and a polytropic constant  $K = K_m = 2.7976 \times 10^{15}$  (Zdunik 2000), which ensures continuity of  $P$  at  $\rho_1$ . The expression for the internal energy is more complicated than in the regular phase,

$$\epsilon = \frac{P}{\rho(\gamma - 1)} + \frac{m_m}{m_u} - 1, \quad (14)$$

where the *mean* atomic mass

$$m_m = m_u \left( 1 - \frac{P_1}{\rho_1} \frac{\gamma_h - \gamma_m}{(\gamma_h - 1)(\gamma_m - 1)} \right). \quad (15)$$

in the mixed phase is determined by demanding that also  $\epsilon$  is continuous at  $\rho_1$ . Here  $P_1$  is the pressure at  $\rho_1$ .

- At high densities  $\rho \geq \rho_2$ , we assume a pure quark matter phase, whose pressure is given by the MIT bag model (Zdunik 2000),

$$P = \frac{1}{3}(\mathcal{E} - \mathcal{E}_2) + P_2, \quad \rho = \rho_2 \left( \frac{4P + \mathcal{E}_2 - 3P_2}{\mathcal{E}_2 + P_2} \right)^{3/4}, \quad (16)$$

where  $\mathcal{E} = \rho(1 + \epsilon)$  is the total energy density of the quark matter<sup>2</sup> and  $P_2$  and  $\mathcal{E}_2$  are the pressure and energy density at  $\rho_2$ , respectively, which again enforces continuity of the EoS at the transition point.

The other set of models uses an microphysical EoS, which exhibits a phase transition to a kaon condensate accompanied by a density discontinuity. The composition of this EoS is as follows:

- For the description of the inner crust (nuclei immersed in neutron and electron gas) and the outer crust (nuclei immersed in electron gas) at densities  $5 \times 10^{10} \text{ g cm}^{-3} \leq \rho \leq$

<sup>1</sup> Note that here we give the EoS in terms of the rest-mass density  $\rho$  (the quantity used by our evolution code) rather than the baryon number density  $n = \rho/m_u$ , where  $m_u = 1.66 \times 10^{-24} \text{ g}$  is the baryon mass.

<sup>2</sup> By assuming that  $\epsilon = \mathcal{E}/\rho - 1$  we can continue to use  $\rho$  and  $\epsilon$  in our system of hydrodynamic equations (9); for a more detailed discussion of this issue, see Abdikamalov et al. (2009).



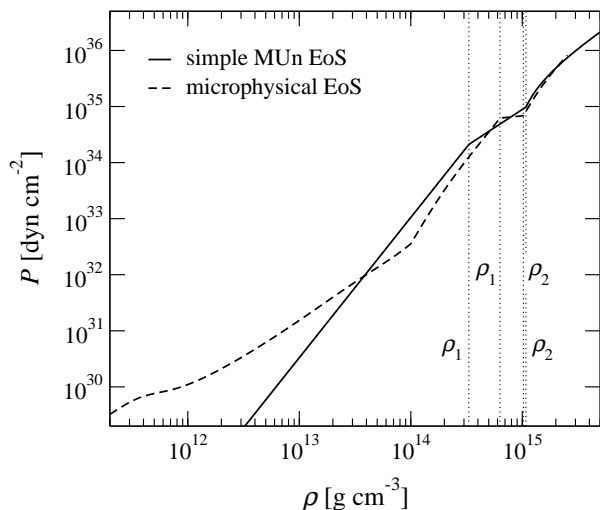


**Figure 1.** Dependence of the pressure  $P$  on the density  $\rho$  for the simple MUn EoS (solid line) and the microphysical EoS (dashed line). The transition densities  $\rho_1$  and  $\rho_2$  for both the MUn EoS and the microphysical EoS are indicated by the dotted lines. Note the domain of zero pressure slope in the microphysical EoS.

$1.5 \times 10^{14} \text{ g cm}^{-3}$  we use the model of Douchin & Haensel (2001). In this model, neutron drip occurs at a density of  $3 \times 10^{11} \text{ g cm}^{-3}$ . The outer crust at densities  $10^8 \text{ g cm}^{-3} \leq \rho \leq 5 \times 10^{10} \text{ g cm}^{-3}$  is modeled by the EoS of Haensel & Pichon (1994). Finally, the low-density envelope with  $\rho < 10^8 \text{ g cm}^{-3}$  is described by the EoS of Baym et al. (1971).

- The constituents of the moderately dense part of the core below the lower end of the density jump at  $\rho_1 = 6.31 \times 10^{14} \text{ g cm}^{-3}$  are neutrons, protons, electrons, and muons. The nucleon component is described by a relativistic mean-field model with scalar self-coupling, as constructed by Zimanyi & Moszkowski (1990). The values of the meson-nucleon coupling constants are  $g_\sigma/m_\sigma = 3.122 \text{ fm}$ ,  $g_\omega/m_\omega = 2.1954 \text{ fm}$ , and  $g_\rho/m_\rho = 2.1888 \text{ fm}$ . The dimensionless coefficients in the cubic and quartic terms in the scalar self-coupling are  $b = -6.418 \times 10^{-3}$  and  $c = 2.968 \times 10^{-3}$ , respectively.

- Although ideally the pressure  $P$  should remain constant across the density jump from  $\rho_1$  to  $\rho_2 = 10.24 \times 10^{14} \text{ g cm}^{-3}$ , in order to avoid numerical problems with the hydrodynamics scheme of the CoCoNuT code we introduce a small linear pressure increase of 10% in this density interval.

- For densities higher than the upper end of the density jump at  $\rho_2$  we consider kaon-condensed matter. The coupling of kaons to nucleons is done according to the model of Glendenning & Schaffner-Bielich (1999) with  $U_K^{\text{lin}} = -110 \text{ MeV}$ .

The properties of these two EoSs are exemplified in Fig. 1, where we plot the dependence of the pressure  $P$  on the rest-mass density  $\rho$ . In the case of the microphysical EoS the approximately constant pressure between  $\rho_1$  and  $\rho_2$  is apparent. In the dense phase, both EoSs have a very similar shape.

Our approach assumes that the fluid is in thermodynamic equilibrium everywhere, even during the dynamic mi-

gration process. The justification of this assumption is given in Appendix A.

As both the simple MUn EoS and the microphysical EoS are barotropic, there is no need to evolve the quantity  $\tau$  in the hyperbolic set of hydrodynamic evolution equations (9, 10). During the recovery of the primitive variables, the associated quantity  $\epsilon$  is simply evaluated from the EoS using the rest-mass density  $\rho$ , and then  $\tau$  is computed straightforwardly according to Eq. (8).

### 3.2 Pre-migration initial models

As shown by Zdunik et al. (2006), for the MUn EoS sequences of uniformly rotating neutron star models with constant baryon mass  $M_0$  exhibit a back bending phenomenon. As shown in Fig. 2, when plotting the total angular momentum  $J$  against the rotation frequency  $f_i$ , for each sequence there exists an unstable segment between a local minimum and maximum of  $J$  (marked by dashed lines). As an isolated neutron star spins down at constant  $M_0$  along this evolutionary path, it will migrate from the last marginally stable configuration (denoted by a circle) to the location on the stable branch with the same total angular momentum  $J$ , provided that the migration proceeds sufficiently rapid that  $J$  is conserved and that the migration does not introduce a deviation of the rotation profile from uniformity. While the first assumption is justified, as the migration is a fast dynamic process, the condition of uniform rotation after the migration has to be verified by numerical simulations. If the rotation profile stays approximately uniform, then the migration path will proceed closely along the dotted lines in Fig. 2. For the microphysical EoS, we find the same back bending phenomenon for sequences of constant  $M_0$ , as presented for a slightly different selection of values for the gravitational mass in Fig. 3.

For our simulation of the dynamic migration due to back bending, we construct initial models that correspond to the last marginally stable configuration marked by circles<sup>3</sup> in Figs. 2 and 3. The properties of these initial models, which utilize the simple MUn EoS (family US) or the microphysical EoS (family UM) are summarized in Table 1. Following the assumption that during the spin down of isolated neutron stars viscous processes drive the rotation profile towards uniformity, we initially assume rigid rotation. Then each model is uniquely specified by its central energy (or alternatively rest-mass) density and its rotation rate  $T_i/|W_i|$ , which is the ratio of rotational energy to gravitational binding energy.

A remarkable property of the marginally stable initial models with the microphysical EoS is that their central density is constant irrespective of the baryon mass (see Table 1). This is a consequence of the first-order phase transition in this EoS with a density jump between  $\rho_1$  and  $\rho_2$ . This transition destabilizes the neutron star exactly when a (theoretically infinitesimally small) core of the dense phase begins

<sup>3</sup> Even though Fig. 3 suggests that for models with the microphysical EoS, the local minimum of  $J$  for the marginally stable models coincides with the local minimum of  $f_i$ , a magnification of this plot reveals that this is not the case and the  $J-f_i$  curves actually are smooth everywhere.

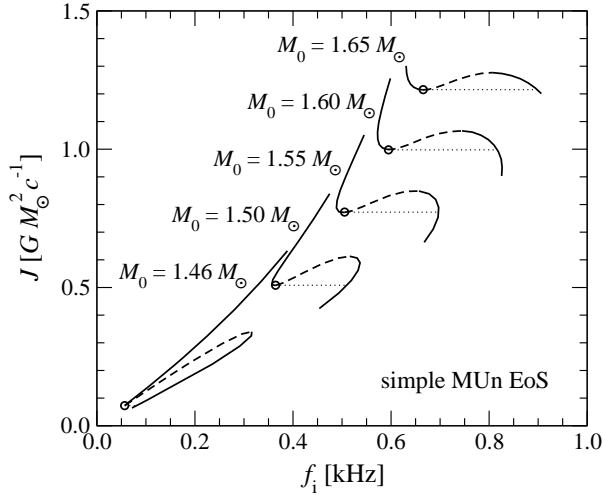


**Figure 2.** Dependence of the total angular momentum  $J$  on the rotation frequency  $f_i$  for uniformly rotating equilibrium models with the simple MUn EoS for various sequences of constant total baryon mass  $M_0$ . Solid/dashed lines specify the stable/unstable segments of the curve. The locations of the marginally stable initial models of the family US are marked by circles, and their transition path to the stable segment assuming conservation of  $J$  and uniform rotation, resulting in a change  $\Delta f$  in rotation frequency, is indicated by dotted lines.

to form in its center<sup>4</sup>. In contrast, the MUn EoS does not possess a first-order phase transition but rather a continuous transition through a mixed phase without density jump. Although the mixed phase also softens the EoS, this softening is not as abrupt as in the microphysical EoS, but “proportional” to the size of the soft core of the mixed phase. Thus the star loses stability only if such a core of sizeable mass is already present in the center, and the exact value of  $\rho_c$  when the marginally stable configuration is reached depends (albeit only weakly) on the mass of the neutron star.

If the hydrodynamic and metric equations could be solved to arbitrarily high precision, then the marginally stable models would already migrate if subjected to an infinitely small perturbation. In our numerical setup, however, truncation and round-off errors together with the small errors from using the CFC approximation of the exact metric equations introduce effects which make it hard to predict if models in the close vicinity of a stable configuration are driven over the edge of stability or not. In order to ensure that in our numerical simulations the initial models undergo the migration robustly in a finite evolution time, we choose to initially apply a finite perturbation to the rest-mass density of the form

$$\Delta\rho = a \sin\left(\frac{r}{r_{\text{atm}}}\pi\right), \quad (17)$$

where  $a = 10^{-3}$  is the perturbation amplitude and  $r_{\text{atm}}$  is

<sup>4</sup> For numerical reasons, in our study the density discontinuity in the microphysical EoS is slightly softened by introducing a small pressure gradient, which leads to a threshold value  $\rho_{c,i} = 9.8 \times 10^{14} \text{ g cm}^{-3}$  that is a bit lower than  $\rho_2$ , where the dense phase begins. The smooth dependence of  $J$  on  $f_i$  discussed in Footnote 3 is also a consequence of this pressure gradient.

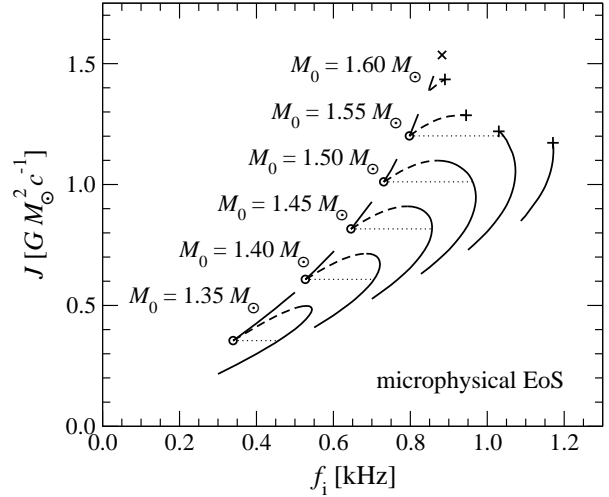


**Figure 3.** Same as Fig. 2 but for models with the microphysical EoS. The locations of the marginally stable initial models of family UM are marked by circles. At the models marked by plus symbols, the Kepler limit interrupts the two sequences with  $M_0 = 1.55 M_\odot$  and  $M_0 = 1.60 M_\odot$ . The transition path of the  $M_0 = 1.55 M_\odot$  sequence is not affected by this discontinuity, while for the  $M_0 = 1.60 M_\odot$  sequence there exists no model on the stable branch with the same  $J$  as the marginally stable one. Note that a fiducial line connecting all marginally stable models with this EoS would end with an  $M_0 = 1.639 M_\odot$  model rotating at the Kepler limit (marked by an x symbol).

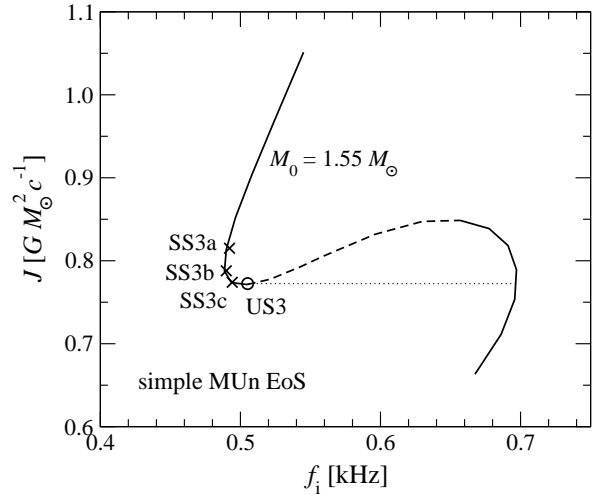


**Figure 4.** Location of the three evolved stable models (marked by crosses) in the  $J$ - $f_i$  diagram for uniformly rotating equilibrium models with the simple MUn EoS and  $M_0 = 1.55 M_\odot$  (see also Fig. 2).

the (latitude dependent) boundary of the neutron star to the surrounding low-density atmosphere. In order to assess the evolutionary behavior of models near the stability limit, we augment model US3 by the three models of family SS3 which are located close to it still on the stable branch, as shown in Fig. 4.

**Table 1.** Summary of the set of migrating marginally stable initial models with the simple MUn EoS (family US) and the microphysical EoS (sequence UM) as well as the stable initial test models with the simple MUn EoS (family SS3).  $M_0$  is the total baryon mass,  $M$  is the total gravitational mass,  $\mathcal{E}_{c,i}$  is the initial central energy density,  $\rho_{c,i}$  is the initial central rest-mass density,  $f_i$  is the initial rotation frequency,  $J$  is the total angular momentum,  $r_{p,i}/r_{e,i}$  is the initial ratio of polar radius to equatorial radius, and  $T_i/|W_i|$  is the initial rotation rate.

Model	$M_0$ [ $M_\odot$ ]	$M$ [ $M_\odot$ ]	$\mathcal{E}_{c,i}$ [ $10^{14}$ g cm $^{-3}$ ]	$\rho_{c,i}$ [ $10^{14}$ g cm $^{-3}$ ]	$\rho_{c,i}/\rho_1$	$\rho_{c,i}/\rho_2$	$f_i$ [kHz]	$J$ [ $GM_\odot^2 c^{-1}$ ]	$r_{p,i}/r_{e,i}$	$T_i/ W_i $ [%]
US1	1.46	1.35	10.22	9.05	2.73	0.84	0.057	0.07	0.998	0.04
US2	1.50	1.39	10.39	9.19	2.77	0.85	0.364	0.51	0.939	1.59
US3	1.55	1.44	10.39	9.19	2.77	0.85	0.505	0.77	0.880	3.19
US4	1.60	1.48	10.22	9.05	2.73	0.84	0.595	1.00	0.829	4.64
US5	1.65	1.53	10.27	9.09	2.74	0.84	0.665	1.22	0.781	6.03
UM1	1.35	1.26	11.03	9.80	2.95	0.91	0.340	0.36	0.953	1.19
UM2	1.40	1.30	11.03	9.80	2.95	0.91	0.528	0.61	0.885	2.98
UM3	1.45	1.35	11.03	9.80	2.95	0.91	0.646	0.82	0.823	4.63
UM4	1.50	1.39	11.03	9.80	2.95	0.91	0.732	1.01	0.766	6.16
UM5	1.55	1.44	11.03	9.80	2.95	0.91	0.798	1.21	0.711	7.58
UM6	1.60	1.48	11.03	9.80	2.95	0.91	0.848	1.39	0.656	8.84
SS3a	1.55	1.44	8.21	7.39	2.23	0.68	0.492	0.82	0.873	3.46
SS3b	1.55	1.44	8.87	7.94	2.39	0.74	0.490	0.79	0.879	3.27
SS3c	1.55	1.44	9.60	8.54	2.57	0.79	0.494	0.77	0.881	3.18

## 4 RESULTS

### 4.1 Dynamics of the migration process

It is well known that the migration of a marginally stable nonrotating spherical neutron star model with a polytropic EoS and adiabatic coefficient  $\gamma = 2$  leads to an expansion of the star (for a numerical simulation of this scenario, see e.g. Font et al. 2002). On the unstable branch, such a model possesses a very compact structure with high central density  $\rho_c$ , while the corresponding model with same baryon mass (and same gravitational mass) on the stable branch has a much smaller value of  $\rho_c$ . Consequently, the entire star significantly expands in size and, after some ring-down pulsations following the initial expansion, settles down to a less dense new equilibrium configuration.

In stark contrast, in our case where two different EoSs are used and the marginally stable initial neutron star models rotate rapidly, a collapse instead of an expansion is expected. This follows directly from the fact that during the migration the rotation frequency  $f$  increases as seen in Figs. 2 and 3 while the total angular momentum is conserved, if the uniform rotation profile is approximately preserved throughout the evolution (which is a good approximation, as later shown in Section 4.2). Still, as in the case of a nonrotating simple polytrope the new equilibrium state – now characterized by an increase in central density compared to the initial value – is overshoot after the primary contraction and is reached only after some ring-down pulsations.

Before we present the collapse dynamics of the marginally stable models that undergo migration, we first discuss the evolution of models from the stable branch that are close to but still sufficiently far from the stability limit, like models SS3a or SS3b. As expected such models remain stable throughout the evolution and simply oscillate around their equilibrium state due to the small perturbation applied initially (see Fig. 5). However, the amplitude of these damped pulsations already grows from model SS3a, which is the one farthest from the marginally stable model US3,

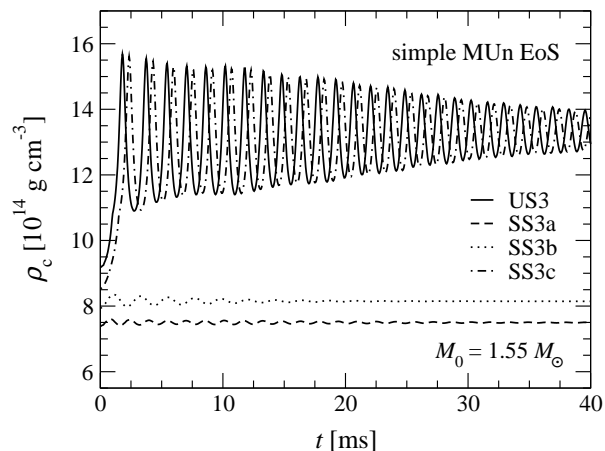


**Figure 5.** Time evolution of the central density  $\rho_c$  for the marginally stable migration model US3 (solid line) and the three stable models SS3a, SS3b, and SS3c (dashed, dotted, and dash-dotted lines, respectively) with the simple MUn EoS and  $M_0 = 1.55 M_\odot$ . Note that model SS3c actually migrates as well, resulting from the finite initial perturbation along with errors introduced by the numerical treatment and the CFC approximation.

to model SS3b that is closer to US3. Interestingly, model SS3c, which lies very near model US3 but is still stable, already undergoes the collapse to higher central densities and more rapid rotation that is associated with the migration to the opposite stable segment. In this case the errors from the numerical treatment and the CFC approximation, and in particular the small but finite initial perturbation suffice to push the neutron star model over the stability limit. Its subsequent central density evolution is very similar to that of the migrating marginally stable model US3, which is also shown in Fig. 5.

When comparing the time evolution of the central density for different models of the same family, as presented in Figs. 6 and 7 for the two EoSs, one recognizes a generic behavior. Within slightly more than 1 ms,  $\rho_c$  increases from

its initial value to a peak of  $\rho_{c,p} \sim 15\text{--}16 \times 10^{14} \text{ g cm}^{-3}$ , and subsequently undergoes damped harmonic oscillations around an asymptotic value that lies between  $\rho_{c,p} \sim 13$  and  $14 \times 10^{14} \text{ g cm}^{-3}$ . The actual numbers for the density increase in the peak and the final value are given in Table 2.

The baryon mass fractions in Table 2 also demonstrate that initially no fluid element in the neutron star has a density above  $\rho_2$ , which is consistent with the values for  $\rho_{c,i}$  given in Table 1, while around 35% and 60% of the stellar mass is at a density above  $\rho_1$  for the MUn EoS and the microphysical EoS, respectively. Later in the evolution, the mass of the star above  $\rho_1$  grows noticeably, and even a significant fraction of  $M_0$  has a density greater than  $\rho_2$ .

When comparing Figs. 6 and 7 it is apparent that while the density oscillations of models with the MUn EoS induced by the migration are somewhat damped, the damping in the models with the microphysical EoS is much stronger<sup>5</sup>. After only a few cycles, the pulsation have died out and  $\rho_c$  (as well as other hydrodynamic and metric quantities at various locations in the star) remain practically constant. By performing simulations with significantly higher grid resolution, we have ensured that this effect is not caused by insufficient numerical accuracy. In addition, since our code utilizes Riemann flux solvers, which can handle discontinuities in the hydrodynamic quantities without problem (see e.g. the relativistic shock tube test presented in Dimmelmeier, Font & Müller 2002a), we can exclude that the pressure jump in the microphysical EoS leads to numerically questionable results. By using a relative convergence criterion of  $10^{-12}$ , we also ascertain that the recovery routine for the primitive quantities is performed to sufficient precision.

When investigating the strong damping of post-migration pulsations in the models of family UM with the microphysical EoS, we find strong evidence that it is a result of a very efficient physical damping mechanism that is reflected in our code. As shown in detail in Appendix B, the kinetic energy stored in the pulsations is dissipated during the compression phase of each pulsation, as matter passes through the density jump from  $\rho_1$  to  $\rho_2$  associated to the first-order phase transition in this EoS. While in reality matter flows into the dense core at supersonic speed and is heated up by shock dissipation, in our simulations the flow remains subsonic. Still, the large density jump results in a rather steep radial inflow velocity profile, leading to numerical dissipation of comparable strength. If the density jump in the EoS is gradually removed, dissipation continuously decreases to the normal level expected for a code based on HRSC methods.

Furthermore, non-equilibrium processes produce entropy via heating. This can be represented by bulk viscosity, but as the corresponding additional dissipation is much smaller than the dissipation caused by the phase transition (see Appendix B3), it is admissible to neglect this mechanism as it is done in our simulations. Another, less important mechanism that is responsible for the damping of post-migration pulsations is the continuous but weak conversion of kinetic energy stored in the pulsations into internal energy by numerical dissipation in the bulk of the star (excluding the parts of the star that are affected by a possible density

jump in the EoS). However, as this process is equally active in all models irrespective of the EoS, in the models with the microphysical EoS it can at most explain damping in a small extent similar to what is observed in the models with the simple MUn EoS, which have a much larger damping time scale. In contrast to some of the rapidly rotating neutron star models discussed by Abdikamalov et al. (2009), which undergo a phase-transition-induced collapse and whose post-collapse pulsations are mainly damped by the shedding of mass from the surface to the atmosphere, we do not find any evidence for the effect of damping by shedding in any of our simulations. The loss of mass across the boundary of our neutron star models remains well below 1% until we deliberately terminate the evolution at  $t_f = 50$  ms.

It is remarkable that according to Table 2 all respective models of family US and UM show a generic “radial” collapse behavior, expressed by a very similar relative increase in central density and fractions of baryon mass above the respective (EoS dependent) transition densities at the collapse peak and the final equilibrium, although the change  $\Delta f$  in rotation frequency along the migration path in the  $J$ - $f_i$  diagram is rather different (see Figs. 2 and 3). For the two investigated EoSs, the balance between pressure, gravitational, and centrifugal forces already lead to almost identical values of these mass fractions and the central density<sup>6</sup> in the marginally stable initial models (see also Table 1), and apparently this does not change during the collapse. We also point out that while the migration lets  $\rho_c$  increase by about 60–70% to its peak value and 40–50% to the final equilibrium value, the *relative* changes in the rotation rate  $T_1/|W_1|$  are comparatively small with values of about 9–12% and 6–7%, respectively.

## 4.2 Final equilibrium states after the migration and spectrum of the pulsations

If the uniformity of the profile rotation is maintained during the dynamic migration and thus the collapsed neutron star in its new final equilibrium state also rotates rigidly, as already speculated by Zdunik et al. (2006), then the migration essentially follows the path marked by the horizontal dotted lines in Figs. 2 and 3, modified only negligibly by a tiny change in  $J$  due to gravitational wave emission (which however cannot be modeled with our formulation of the metric equations).

With our fully dynamic code we are now able to test this assumption of preservation of the rotation profile during the collapse and the subsequent ring-down. In Figs. 8 and 9 the radial profiles of the rotation velocity  $v_\varphi$  in the equatorial plane are plotted both for the initial model (where they obviously scale linearly with radius  $r$ ) and at the end of the evolution at 50 ms for the simple MUn EoS and the microphysical EoS, respectively. In both cases the degree of differential rotation created by the migration is rather small, although the central density increases by up to 50%. It is actually possible to approximate the final rotation profile rather accurately by an analytic law for the specific angular momentum  $j$  (see e.g. Komatsu, Eriguchi & Hachisu 1989a),

<sup>5</sup> Note the different time scales in the two figures!

<sup>6</sup> In the case of the microphysical EoS,  $\rho_{c,i}$  is indeed independent of  $M_0$  as explained in Section 3.2.



**Table 2.** Summary of the migration dynamics for models with the simple MUn EoS (family US) and the microphysical EoS (sequence UM).  $\rho_{c,p}$  is the peak central density obtained at the first collapse peak, while  $\rho_{c,f}$  is the asymptotic value for the central density after the pulsations have died out and  $\rho_{c,fb}$  is the central density of the corresponding equilibrium model with the same value of  $J$  from the stable branch in Fig. 2 and 3, respectively (for model UM6 that corresponding model is beyond the Kepler limit).  $M_{0,\rho>\rho_{1/2,i}}/M_0$ ,  $M_{0,\rho>\rho_{1/2,p}}/M_0$ , and  $M_{0,\rho>\rho_{1/2,f}}/M_0$  are fractions of baryon mass above the (EoS dependent) transition densities  $\rho_1$  and  $\rho_2$  at the initial time, the time of the maximum central density peak, and averaged at late evolution times, respectively.  $|h|_{\max}$  is the maximum gravitational wave strain, with the values without taking into account mode resonance effects given in parentheses.

Model	$\rho_{c,p}$ [ $10^{14} \frac{\text{g}}{\text{cm}^3}$ ]	$\frac{\rho_{c,p}}{\rho_{c,i}}$	$\rho_{c,f}$ [ $10^{14} \frac{\text{g}}{\text{cm}^3}$ ]	$\rho_{c,fb}$ [ $10^{14} \frac{\text{g}}{\text{cm}^3}$ ]	$\frac{M_{0,\rho>\rho_{1,i}}}{M_0}$	$\frac{M_{0,\rho>\rho_{1,p}}}{M_0}$	$\frac{M_{0,\rho>\rho_{1,f}}}{M_0}$	$\frac{M_{0,\rho>\rho_{2,p}}}{M_0}$	$\frac{M_{0,\rho>\rho_{2,f}}}{M_0}$	$ h _{\max}$
US1	16.24	1.796	13.48	13.69 (2%)	0.35	0.71	0.58	0.35	0.17	0.48 (0.12)
US2	15.99	1.741	13.33	13.62 (2%)	0.35	0.70	0.58	0.33	0.17	3.69 (2.81)
US3	15.69	1.708	13.33	13.55 (2%)	0.35	0.68	0.57	0.31	0.17	7.97 (3.94)
US4	15.33	1.725	13.48	13.50 (1%)	0.33	0.66	0.56	0.29	0.16	4.35
US5	14.94	1.644	13.09	13.45 (3%)	0.34	0.64	0.54	0.26	0.15	4.62
UM1	16.84	1.718	14.31	14.28 (1%)	0.01	0.46	0.32	0.43	0.28	4.50 (1.42)
UM2	16.37	1.670	14.11	14.28 (1%)	0.01	0.45	0.31	0.41	0.28	6.90 (4.25)
UM3	16.16	1.649	14.11	14.27 (1%)	0.01	0.43	0.30	0.40	0.27	6.69 (5.90)
UM4	16.00	1.633	14.11	14.27 (1%)	0.01	0.42	0.29	0.38	0.26	6.50
UM5	15.83	1.615	13.92	14.29 (3%)	0.01	0.40	0.28	0.36	0.25	6.89
UM6	15.61	1.597	13.92	—	0.01	0.38	0.27	0.35	0.24	7.57

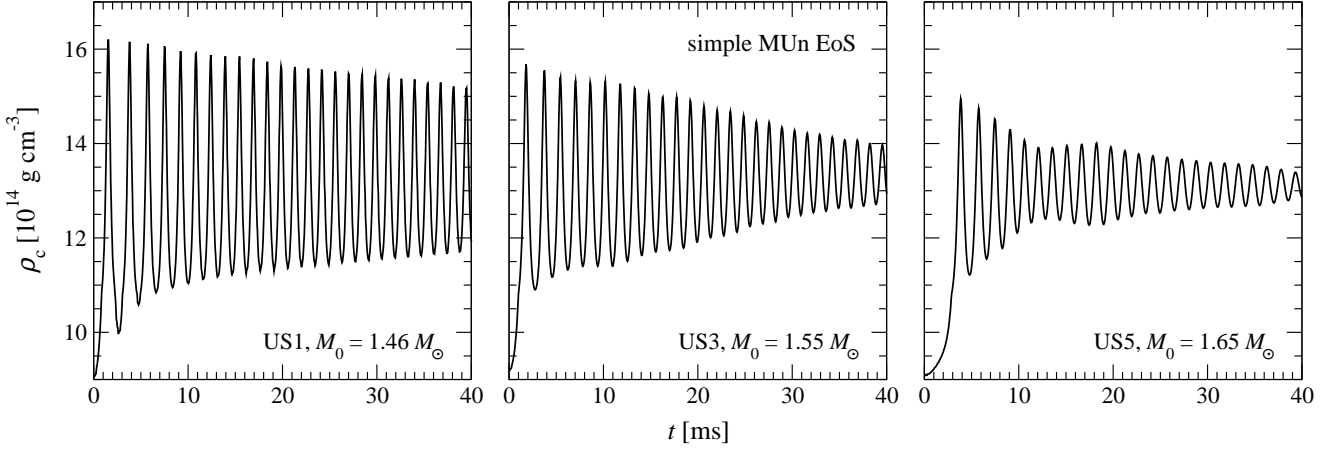


**Figure 6.** Time evolution of the central density  $\rho_c$  for three migration models of family US with the simple MUn EoS.

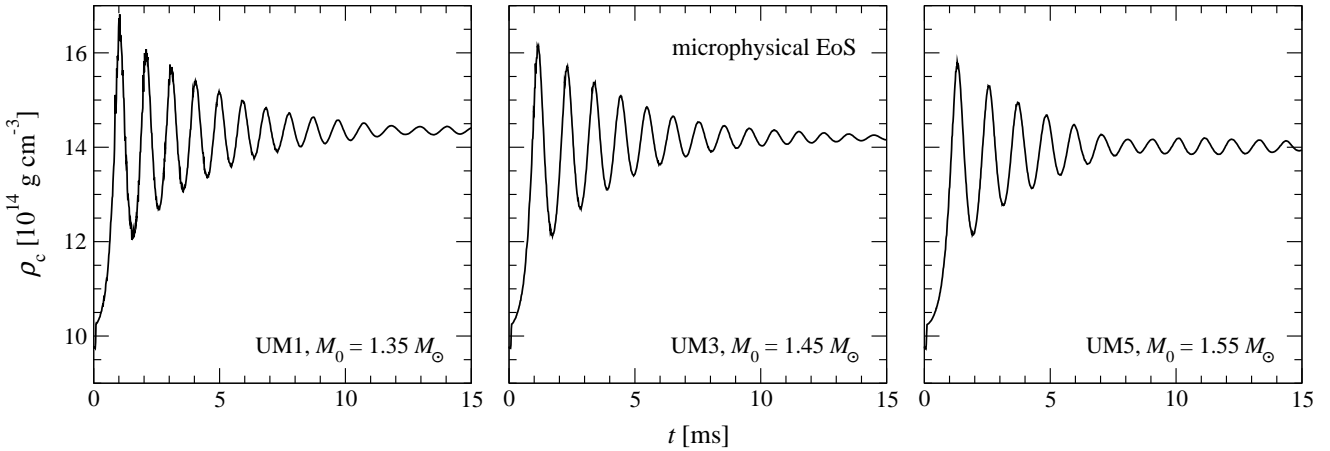


**Figure 7.** Time evolution of the central density  $\rho_c$  for three migration models of family UM with the microphysical EoS.

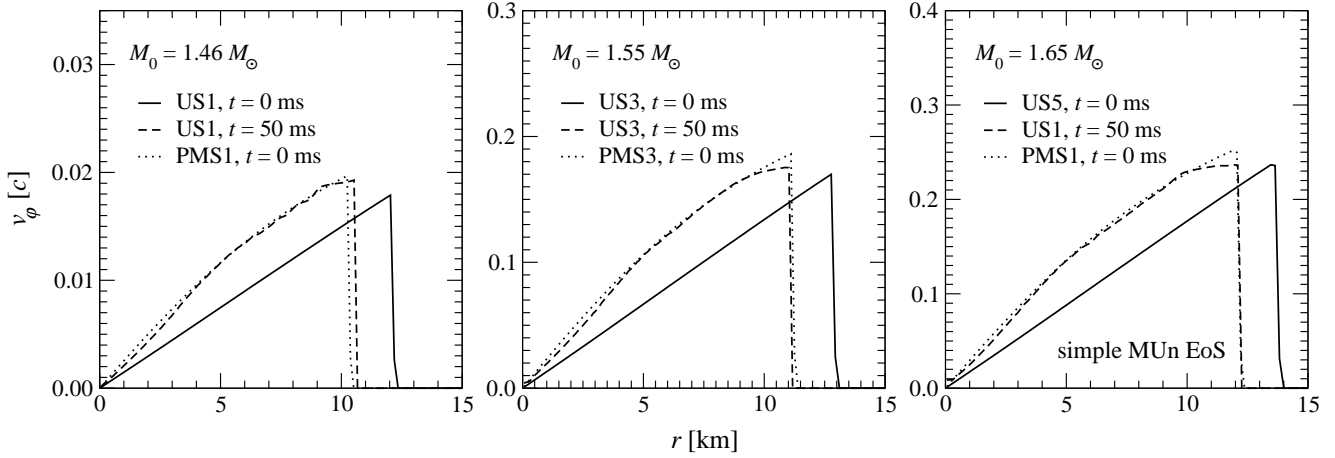


**Figure 8.** Radial profiles in the equatorial plane of the rotation velocity  $v_\phi$  for three models with the simple MUn EoS. The solid and dashed lines are at the initial and final evolution time, respectively, for migration models of family US, while the dotted lines show  $v_\phi$  at the initial evolution time for stable post-migration models of family PMS.

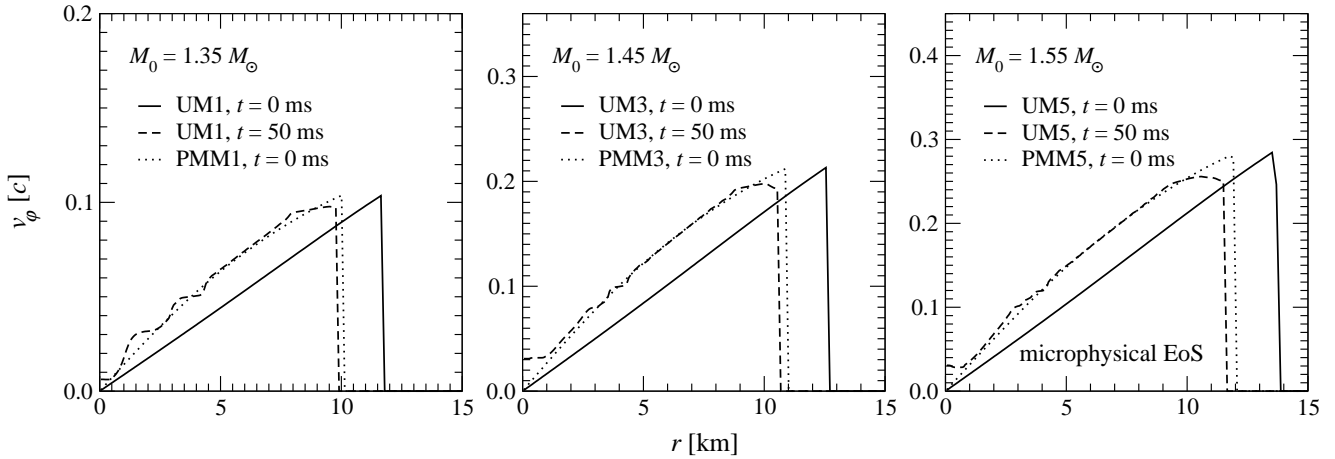


**Figure 9.** Radial profiles in the equatorial plane of the rotation velocity  $v_\phi$  for three models with the microphysical EoS. The solid and dashed lines are at the initial and final evolution time, respectively, for migration models of family UM, while the dotted lines show  $v_\phi$  at the initial evolution time for stable post-migration models of family PMM.

$$j = A^2(\Omega_c - \Omega), \quad (18)$$

where  $A$  parametrizes the degree of differential rotation (stronger differentiability with decreasing  $A$ ) and  $\Omega_c$  is the value of the angular velocity  $\Omega$  at the center. This simple relation is widely used in general relativistic hydrodynamics to model differential rotation in compact stars. The differential rotation length scale  $A$  can be put into relation with the equatorial radius  $r_e$  in isotropic coordinates by defining the dimensionless quantity  $\hat{A}$ . If  $\hat{A} \ll 1$ , then the rotation profile is very differential (with a larger specific angular momentum distribution at small distances to the rotation axis), while  $\hat{A} \gg 1$  leads towards the limit of uniform rotation. For the approximated post-migration rotation curves of our models we find values  $\hat{A}$  that are always larger than 1 and reach almost 3 for some models (as presented in Table 3) which confirms the conclusions from the visual analysis of Figs. 8 and 9. Despite the creation of some differential rotation during the dynamic migration, the post-migration models are thus rather well approximated by the equilibrium models on the stable branch in the  $J$ - $f_1$  diagram (given by the right end

points of the dotted lines in Figs. 2 and 3) that have the same value of  $J$  as the marginally stable initial model. Further evidence for this conclusion is given by the observation that the final central density  $\rho_{c,f}$  of any post-migration model differs from the central density  $\rho_{c,sb}$  of the corresponding model on the stable branch by at most 3% (see Table 2).

Although the pulsations triggered by the initial collapse are only slowly damped for the models with the simple MUn EoS, they will eventually die out, and a stable equilibrium will be reached. With the knowledge of an approximate analytic solution for the final rotation profile we are thus able to compute stable equilibrium models which should closely match the post-migration configurations obtained from the dynamic evolution. For this we utilize the same method employed to construct the marginally stable initial models for the migration simulations, with the important difference that now slightly differential rotation profiles with the values for  $\hat{A}$  from Table 3 are needed. Using the same EoS as for the respective migration model, only one additional parameter to uniquely determine each of these new equilibrium models

is left, like e.g. the baryon mass  $M_0$ , the gravitational mass  $M$ , the total angular momentum  $J$ , or the central (energy or rest-mass) density  $\mathcal{E}_c$  or  $\rho_c$ .

For practical reasons we chose  $\rho_c$  as the parameter of choice, which we select such that it equals the value of  $\rho_{c,f}$  in Table 2. With this method for each migration model of the two families US and UM an accompanying equilibrium model that resembles the final state is constructed. We label the resulting families of approximative post-merger models by PMS and PMM for the simple MUn EoS and the microphysical EoS, respectively. The parameters for these models are summarized in Table 3. The excellent agreement in both  $M_0$  and  $M$  as well as  $J$  between the respective members of families of marginally stable initial models and post-migration equilibrium models (compare the values given in Tables 1 and 3) illustrates the validity of this approach<sup>7</sup>. Therefore, it is possible to very accurately describe the neutron star at the end point of the migration by a simple equilibrium model obeying an analytic rotation law, which facilitates a variety of ways to further analyze the outcome of the migration process.

This method even works for the peculiar model UM6 with the microphysical EoS, whose marginally stable initial configuration has no counterpart on the stable branch at constant  $J$  and respectively higher  $f$  in the  $J$ - $f_i$  diagram for uniformly rotating equilibrium models in Fig. 3, as models in this segment of the sequence are beyond the Kepler limit. It is noteworthy that model UM5 exhibits the same migration dynamics as the other models of its family, without contracting to excessively high densities (or even collapsing a black hole) or being subject to mass shedding. The small (albeit nonzero) development of a differential rotation profile during the migration suffices to create a stable final equilibrium state that is located within the Kepler limit. We are thus able to construct the corresponding post-migration equilibrium model PMM6, whose value  $\dot{A} = 2.5$  for the differential rotation parameter is typical for family UM (see Table 3).

We find that even the extremal marginally stable model with  $M_0 = 1.639 M_\odot$ , which already initially rotates at the Kepler limit (see Fig. 3) migrates as the other models to a stable, differentially rotating equilibrium configuration without mass shedding. The segments of the  $M_0 = \text{const.}$  sequences in the  $J$ - $f_i$  diagram that are beyond the Kepler limit are therefore irrelevant for the actual migration process, as the fiducial migration path indicated by dotted lines in that figure requires exact preservation of uniform rotation throughout the migration, which is not obeyed during a fully dynamic evolution. We note that the marginally stable models with the simple MUn EoS also end at the Kepler limit with a model that, however, has a rather large baryon mass  $M_0 = 1.899 M_\odot$ . As this model's total angular momentum  $J = 2.30$  is very large as well, we refrain from including it in the respective  $J$ - $f_i$  diagram in Fig. 2.

### 4.3 Analysis of the pulsations modes

A clear example of the benefit of being able to approximate the final post-migration states of our models by simple equilibrium configurations is the possibility to comprehensively examine the quasi-normal pulsation modes triggered by the migration by perturbing those respective post-migration equilibrium models. It is difficult in some cases to unambiguously identify the mode nature and its eigenfunction structure directly from the dynamic simulation of the migration itself, as both the absolute and relative excitation of the various modes is not under control, and the pulsation spectrum is rather complex (see the solid lines in Fig. 10). In contrast, in the corresponding equilibrium models, by applying a initially a selection of small trial eigenfunctions of defined parity, we can excite a range of particular quasi-normal modes in the linear regime with controlled amplitude. For  $l = 0$  oscillations, we set the radial velocity to

$$v_r = a \sin\left(\frac{r}{r_{\text{atm}}}\pi\right) \quad (19)$$

with amplitude  $a = -0.005$ , and for  $l = 2$  we set the angular velocity to

$$v_\theta = a \sin\theta \cos\theta \sin\left(\frac{r}{r_{\text{atm}}}\pi\right) \quad (20)$$

with  $a = 0.01$ . In order to improve the results obtained from these perturbed equilibrium models even more, in difficult cases<sup>8</sup> we apply a further recycling run for each of the main quasi-normal modes, which are the fundamental quasi-radial  $F$ -mode, the fundamental quadrupolar  ${}^2f$ -mode, and their respective harmonics, the  $H_1$ -mode and the  ${}^2p_1$ -mode (for this we essentially follow the technique described in Dimmelmeier, Stergioulas & Font 2006). This method facilitates an accurate extraction of both the frequency and the eigenfunction of each mode, and thus allows us to clearly identify the mode nature. The improvement in the clarity of the pulsation spectrum from using the trial eigenfunctions alone is apparent from the dashed lines in Fig. 10, where  $l = 0/2$  parity was used in the left/right panel, respectively, as quasi-radial modes are predominantly visible in quantities like the density, while quadrupolar modes are prominent for instance in the waveform.

The frequencies of the four main quasi-normal modes (the fundamental  $F$ -mode and  ${}^2f$ -mode, and the harmonic  $H_1$ -mode and  ${}^2p_1$ -mode) extracted from the migration models and the respective values from their respective recreated post-migration equilibrium configurations excited by small amplitude perturbations along with the major nonlinear self-couplings are presented in Table 4 for the simple MUn EoS and in Table 5 for the microphysical EoS. Except for the fundamental quasi-radial  $F$ -mode, which nevertheless shows satisfactory agreement, the equilibrium models reproduce the frequencies of those modes to excellent accuracy, with relative differences of typically less than 5%. For the simple MUn EoS only in few cases the frequency of quasi-normal or nonlinear modes could not be identified (marked by dashes in Table 4), presumably because of the

<sup>7</sup> We note that it makes no sense to locate these post-migration equilibrium models in the  $J$ - $f_i$  diagram in Figs. 2 and 3, as they possess a small but non-negligible amount of differential rotation.

<sup>8</sup> For rapid rotation, the quasi-radial modes acquire a strong quadrupolar contribution, making an unambiguous identification (particularly of the first harmonic mode  $H_1$ ) a demanding task.

**Table 3.** Summary of the set of stable post-migration initial models with the simple MUn EoS (family PMS) and the microphysical EoS (family PMM).  $f_{c,i}$  is the central rotation frequency,  $\hat{A}$  is the differential rotation length scale, and the other quantities are explained in Table 1. Note that as required, the quantities  $M_0$ ,  $M$  and  $J$  are almost identical to the respective marginally stable models.

Model	$M_0$ [ $M_\odot$ ]	$M$ [ $M_\odot$ ]	$\mathcal{E}_{c,i}$ [ $10^{14}$ g cm $^{-3}$ ]	$\rho_{c,i}$ [ $10^{14}$ g cm $^{-3}$ ]	$f_{c,i}$ [kHz]	$J$ [ $GM_\odot^2 c^{-1}$ ]	$\hat{A}$	$r_{p,i}/r_{e,i}$	$T_i/ W_i $ [%]
PMS1	1.45	1.35	15.93	13.53	0.089	0.07	2.7	0.998	0.04
PMS2	1.50	1.39	15.81	13.44	0.549	0.50	2.8	0.930	1.66
PMS3	1.56	1.44	15.67	13.33	0.810	0.81	2.5	0.850	3.72
PMS4	1.59	1.47	15.53	13.23	0.882	0.97	2.7	0.810	4.77
PMS5	1.66	1.54	15.34	13.09	1.025	1.27	2.5	0.740	6.76
PMM1	1.35	1.26	16.73	14.34	0.498	0.34	2.5	0.950	1.18
PMM2	1.40	1.30	16.60	14.23	0.763	0.58	2.5	0.880	2.91
PMM3	1.45	1.34	16.51	14.18	0.945	0.80	2.5	0.810	4.73
PMM4	1.50	1.39	16.38	14.08	1.063	0.99	2.5	0.750	6.34
PMM5	1.54	1.43	16.30	14.01	1.118	1.15	2.7	0.700	7.60
PMM6	1.59	1.47	16.11	13.87	1.195	1.34	2.5	0.650	9.01

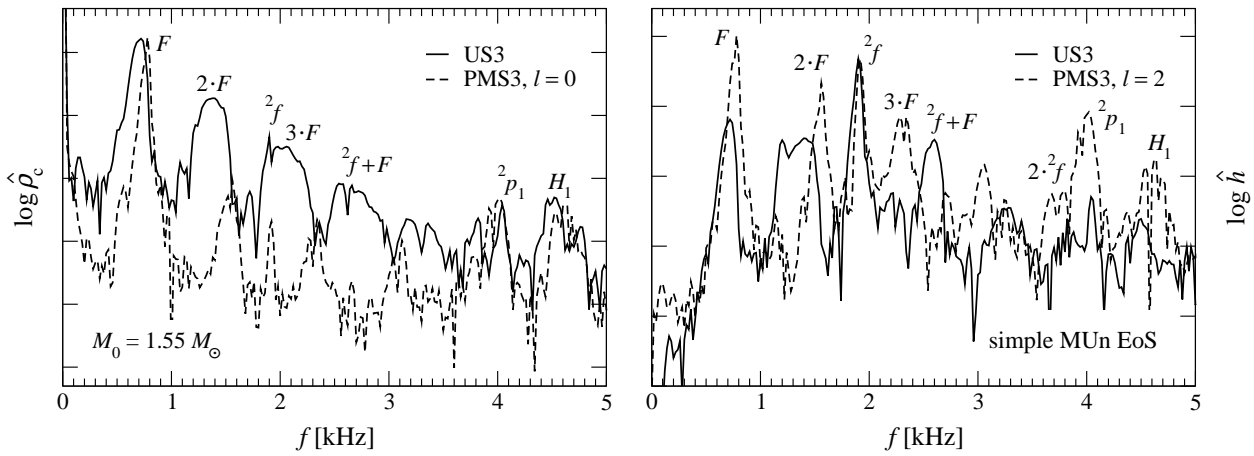


**Figure 10.** Logarithmic frequency spectrum (i.e. Fourier transform as indicated by the hat symbol) of the time evolution of the central density  $\rho_c$  (left panel) and the gravitational wave strain  $h$  (right panel) for the migration model US3 (solid line) and the associated post-migration equilibrium model PMS3 (dashed line, excited with an  $l = 0/2$  trial eigenfunction for  $\rho_c/h$ , respectively) with the simple MUn EoS. The vertical scale is one order of magnitude per tick mark. Several prominent quasi-normal modes and their nonlinear couplings are marked. The data have been scaled such that the peaks of the  $F$ -mode (left panel) and the  $2f$ -mode (right panel) have the same height for the two models US3 and PMS3.

**Table 4.** Frequencies for quasi-normal modes and some of their nonlinear self-couplings for the migration models of the family US and the post-migration equilibrium models of the family PMS with the simple MUn EoS.  $f_F$ ,  $f_{2f}$ ,  $f_{H_1}$ , and  $f_{2p_1}$  are the frequencies of the fundamental quasi-radial mode, the fundamental quadrupolar mode, and their respective first harmonics, while the other modes are nonlinear self-couplings. For the quasi-normal modes the relative differences in frequency between the model of the US and PMS family are also given. For some models, particular modes could not be extracted with sufficient confidence, probably due to interaction with nearby other modes.

Model	$f_F$ [kHz]		$f_{2f}$ [kHz]		$f_{H_1}$ [kHz]		$f_{2p_1}$ [kHz]		$f_{2\cdot F}$ [kHz]	$f_{3\cdot F}$ [kHz]	$f_{2\cdot 2f}$ [kHz]
US1	0.713		1.817		4.792		4.173		1.407	2.107	3.625
PMS1	0.848	19%	1.893	4%	4.901	3%	4.231	1%	1.705	2.554	3.795
US2	0.723		1.867		—		4.320		1.429	2.140	3.665
PMS2	0.794	10%	1.907	2%	4.748	—	4.166	2%	1.609	2.412	3.824
US3	0.728		1.909		4.483		4.048		1.389	2.070	3.817
PMS3	0.777	7%	1.924	1%	4.619	3%	4.024	1%	1.562	2.350	3.870
US4	0.716		1.926		4.499		3.875		1.421	2.131	—
PMS4	0.730	2%	1.914	1%	4.536	1%	3.893	5%	1.456	2.192	—
US5	0.663		1.922		4.517		3.673		1.318	1.974	—
PMS5	0.617	7%	1.890	2%	4.464	1%	3.635	1%	1.238	1.877	—



**Table 5.** Frequencies for quasi-normal modes and some of their nonlinear self-couplings for the migration models of the family UM and the post-migration equilibrium models of the family PMM with the microphysical MUn EoS.  $f_F$  and  $f_{2f}$  are the frequencies of the fundamental quasi-radial mode and the fundamental quadrupolar mode, while the other modes are nonlinear self-couplings. For the quasi-normal modes the relative differences in frequency between the model of the UM and PMM family are also given. For this model family, the strong damping of pulsations prohibits a clear identification of the harmonics.

Model	$f_F$ [kHz]		$f_{2f}$ [kHz]		$f_{2F}$ [kHz]	$f_{3F}$ [kHz]
UM1	1.061		2.080		2.122	3.030
PMM1	1.156	9%	2.081	1%	2.286	3.395
UM2	1.080		2.100		2.160	3.161
PMM2	1.051	3%	2.084	1%	2.102	3.153
UM3	1.000		2.139		2.000	3.031
PMM3	1.100	10%	2.103	2%	2.182	3.280
UM4	0.960		2.129		1.920	2.741
PMM4	0.966	1%	2.112	1%	1.941	2.701
UM5	0.942		2.141		1.884	2.882
PMM5	1.061	13%	2.122	1%	2.143	3.222
UM6	0.845		2.120		1.700	2.521
PMM6	0.824	2%	2.080	2%	1.660	2.449

interaction with another sufficiently strongly excited mode nearby in the spectrum, while for the microphysical EoS neither of the harmonics can be extracted unambiguously (thus we refrain from presenting them in Table 5).

A comparison of the mode spectra of the migrating model US3 with those of the corresponding perturbed post-migration equilibrium model PMS3 in Fig. 10 also exhibits that the collapse associated with the dynamic migration in model US3 excites several nonlinear couplings between quasi-normal modes, with some of them being self-couplings like for instance the  $2 \cdot F$ -mode at twice the frequency of the fundamental quasi-radial  $F$ -mode. Abdikamalov et al. (2009) have also reported such strong nonlinear mode excitation in their simulations of rotating neutron star models that collapse to hybrid quark stars following a phase transition to quark matter in the core. In contrast, in the only slightly perturbed model PMS3 these nonlinear modes are very weak or even not present at all. They make the same observation – a strong presence of nonlinear modes in the spectrum of the migration models and an efficient suppression of such modes in the respective equilibrium models – in all members of the two model families, irrespective of the EoS used. We therefore speculate that in a sufficiently strong dynamic gravitational collapse, one can expect that nonlinear pulsations modes of non-negligible amplitude are excited, independent of the physical mechanism that activates the collapse.

A peculiar property of all models of family US with the simple MUn EoS is revealed by a comparison of the evolution of their density structure during the migration and the ring-down with the extracted density eigenfunction  $\rho_F$  of the  $F$ -mode, which is always the mode that contains the largest pulsation energy (as e.g. shown by the strong peak in the spectrum of  $\rho_c$  in the left panel of Fig. 10). We observe that, as expected, the density in the migrating neutron star

changes during the evolution everywhere in the star. Surprisingly, however, the density remains practically constant at the two-dimensional surface where  $\rho = \rho_1$  initially, as demonstrated for the two radial density profiles of model US5 along the equatorial plane and the polar axis in the left panel of Fig. 11, presented at both  $t = 0$  and 50 ms. Apparently, while  $\rho_c$  jumps from well below to well above  $\rho_2$ , the (angular dependent) location where  $\rho = \rho_1$  stays at almost the same radius. The plot of the corresponding density eigenfunction profiles in the center panel of Fig. 11 then shows that  $\rho_F$  has a node virtually at the same location. In the right panel of Fig. 11 this behavior is summarized by plotting the maximum range during the entire evolution time of (rotationally symmetric) surfaces where  $\rho = \rho_2$  (closest to the center, with a large variation and a minimum range of  $r = 0$  as  $\rho < \rho_2$  initially in the star), where  $\rho = \rho_1$  (which lies in a very narrow interval), and where  $\rho = \rho_{\text{atm}}$  (i.e. the boundary of the star which again changes its extent significantly). The close proximity of the surface with  $\rho = \rho_1$  to the nodal surface of the eigenfunction  $\rho_F$  is striking. We speculate that if nodal surface is “pinned down” where the EoS qualitatively changes its properties at the density  $\rho_1$ , which is also the location where  $\partial P / \partial \rho$  becomes discontinuous. Apart from this attempt of explanation we are not able to give a compelling reason for this property of the US models, but it is obvious that regarding the main pulsation mode the migrating star decomposes into two separate domains with an interface at  $\rho = \rho_1$ , each of them pulsating coherently, but with opposite phase.

Similarly, we find that the models of family UM with a microphysical EoS exhibit a nodal surface for the  $F$ -mode that is approximately constant in space throughout the migration and the subsequent ring-down, although here the surface expands a bit during the first phase of the migration. However, the (again approximately constant) density in the neutron star model corresponding to this nodal surface now is not a distinguished location in the microphysical EoS, being for instance significantly smaller than  $\rho_1$ , where the domain with zero pressure slope starts. Unlike in the models with the simple MUn EoS, in the models with the microphysical EoS the eigenfunction topology is apparently not influenced by any transition density of the EoS.

In passing, we point out that in contrast to the rotating neutron star models by Lin et al. (2006) that undergo a mini-collapse due to a phase transition in the EoS leading to a formation of a quark matter core, our models do not develop significant convection after the initial contraction. This would be easily observable both as a strong low-frequency contribution much below 1 kHz in the spectrum shown in Fig. 10 and as a step-like pattern corresponding to the convection cells in the radial rotation velocity profiles in Figs. 8 and 9. Abdikamalov et al. (2009) have shown that for such a phase-transition-induced collapse with the particular EoS treatment of Lin et al. (2006) the convection is caused by a significant negative entropy gradient, which is not present in our models.

#### 4.4 Emission of gravitational waves and mode resonance

While the increase in density resulting from the migration is quite uniform for all members of each model family, the

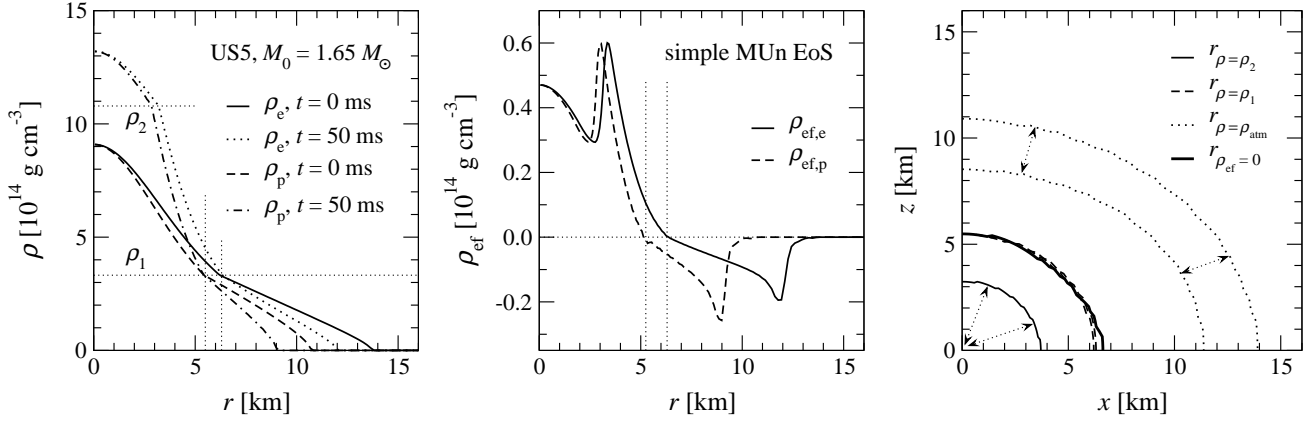


**Figure 11.** Density topology of the most rapidly rotating migration model US5 of family US with the simple MUn EoS. In the left panel the radial profiles of the densities  $\rho_e$  in the equatorial plane and  $\rho_p$  along the polar axis are shown at the initial and final evolution time, respectively. The horizontal dotted lines mark the transition densities  $\rho_1$  and  $\rho_2$ , while the vertical dotted lines specify the radius where  $\rho_e$  and  $\rho_p$  equal  $\rho_1$  apparently independent of the evolution time. In the center panel the  $F$ -mode density eigenfunction  $\rho_{F,e}$  in the equatorial plane and  $\rho_{F,p}$  along the polar axis is plotted. The vertical dotted lines indicate the respective nodes. In the right panel we show the range (symbolized by arrows) for the radial location of the surface where the density  $\rho$  equals  $\rho_2$ ,  $\rho_1$ , and the atmosphere cutoff density  $\rho_{\text{atm}}$  during the evolution, as well as the nodal surface of  $\rho_F$ . Here  $x = r \sin \theta$  and  $z = r \cos \theta$  are the Cartesian coordinates.

strength of gravitational wave emission, which is sensitive to the rotation frequency, is expected to vary as the initial value of  $f$  and the change  $\Delta f$  during the collapse varies among different models. The dependence of the waveform on the rotation rate is clearly revealed in the gravitational radiation waveform plots presented in Figs. 12 and 13 for three selected models of each of the two families US and UM, respectively. The according (absolute) peak amplitudes  $|h|_{\text{max}}$  of the waveforms are summarized in Table 2. The main emission modes are the  $2f$ -mode and, for rapidly rotating models, also the  $F$ -mode.

It is remarkable for this migration scenario that  $|h|_{\text{max}}$  apparently does not monotonically depend on either  $f_i$  or  $T_i/|W_i|$  (see e.g. the plot in the top panels of Fig. 14 for model family US and Fig. 15 for model family UM). An instructive example is also the relatively slowly rotating model US1 (see left panel of Fig. 12), where the maximum waveform amplitude during the initial collapse phase of the migration, which lasts at most 2 ms, is around  $10^{-22}$  at a distance of 10 kpc from the source. Considerably later, at  $t \sim 5$  ms, already well in the ring-down phase, the amplitude gradually increases until it saturates at times after  $\sim 10$  ms with a maximum  $|h|_{\text{max}} \sim 5 \times 10^{-22}$ . Finally, after that the amplitude of the quasi-periodic waveform's envelope decays as expected (see also the qualitatively similar waveform of model UM1 in the left panel of Fig. 13).

A very similar behavior was also found in recent simulations of rotating neutron star models which collapse due to an EoS phase transition (Abdikamalov et al. 2009). In that work it was shown that nonlinear modes can vigorously boost the emission of gravitational waves if they are in resonance with an efficiently emitting quadrupolar mode like the  $2f$ -mode, provided that both the frequencies of those two modes are in close proximity and the nonlinear mode contains a substantial amount of pulsation kinetic energy (see also Eardley 1983; Dimmelmeier, Stergioulas & Font 2006). While in the models of Abdikamalov et al. (2009) the nonlinear mode which drives the mode resonance is the  $2 \cdot F$ -mode, the mode to be considered here is the  $3 \cdot F$ -mode for

the models with the simple MUn EoS and the  $2 \cdot F$ -mode for the ones with the microphysical EoS, as suggested by the frequencies given in Tables 4 and 5, respectively.

Indeed Figs. 14 and 15 show the connection between the proximity of these potentially resonating modes and the maximum waveform amplitude  $|h|_{\text{max}}$  for all migrating models considered here. By evaluating  $|h|_{\text{max}}$  on the one hand only in a time window close to the time of maximum compression (i.e. at the end of the dynamic initial collapse phase before mode resonance can develop; dashed line) and on the other hand for the full waveform (solid line), the enhancement of gravitational wave emission by resonance can be quantified. For the models with a microphysical EoS of family UM in Fig. 15, both the absolute and the relative amplification of the waveform amplitude (see top and center panel, respectively) is clearly strongest when the  $2 \cdot F$ -mode is closest in frequency to the  $2f$ -mode. This happens at low rotation, while for rapid rotation we detect no imprint of mode resonance in the waveform and  $|h|_{\text{max}}$  obtained close to the time of maximum compression is the global maximum. The models with a simple MUn EoS presented in Fig. 14 reveal a slightly more complicated behavior. Again the slowest rotator exhibits the strongest relative increase of  $|h|_{\text{max}}$  by mode resonance (see center panel), albeit from a very small absolute level (see top panel). As rotation grows and the frequencies of the  $2 \cdot F$ -mode and the  $3 \cdot F$ -mode approach each other, the effects of the resonance on  $|h|_{\text{max}}$  become apparent. However, in the rapid rotation limit mode resonance again ceases (as for the models of family UM), although in family US the frequencies of the two relevant modes are now in close proximity. Here the waveform again possess a regularly damped sinusoidal pattern.

For such rapidly rotating models, we find that the peaks associated to the  $2f$ -mode and the  $3 \cdot F$ -mode (for family US) or the  $2 \cdot F$ -mode (for family UM) are clearly separated also during the interval from 5 to 15 ms. Additionally, the respective nonlinear self-coupling of the  $F$ -mode is excited to a much lesser degree than in slower rotating models with mode resonance, and thus carries less transferable

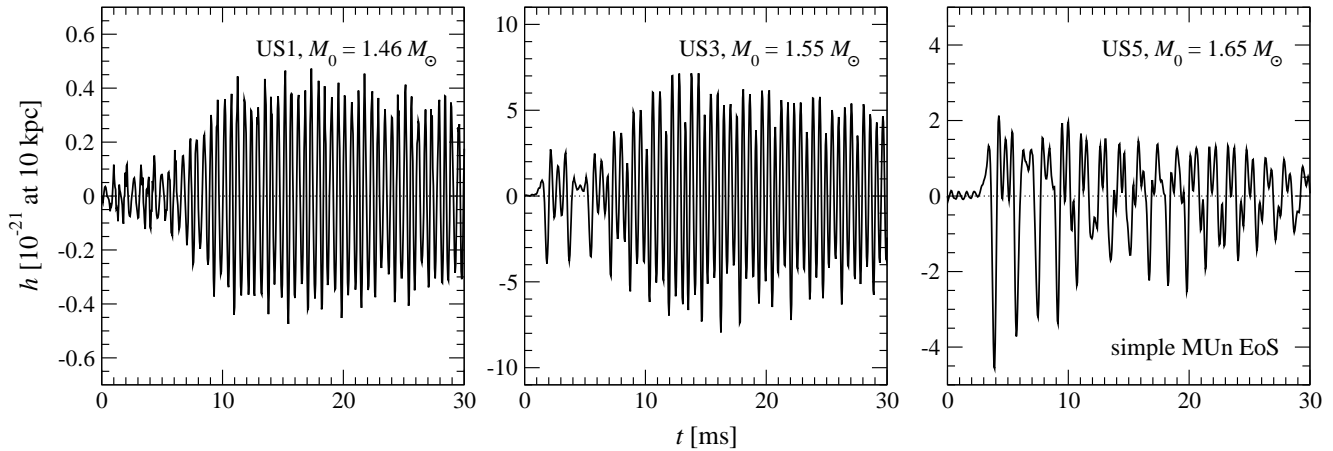


**Figure 12.** Time evolution of the gravitational wave strain  $h$  for three migration models of family US with the simple MUn EoS.

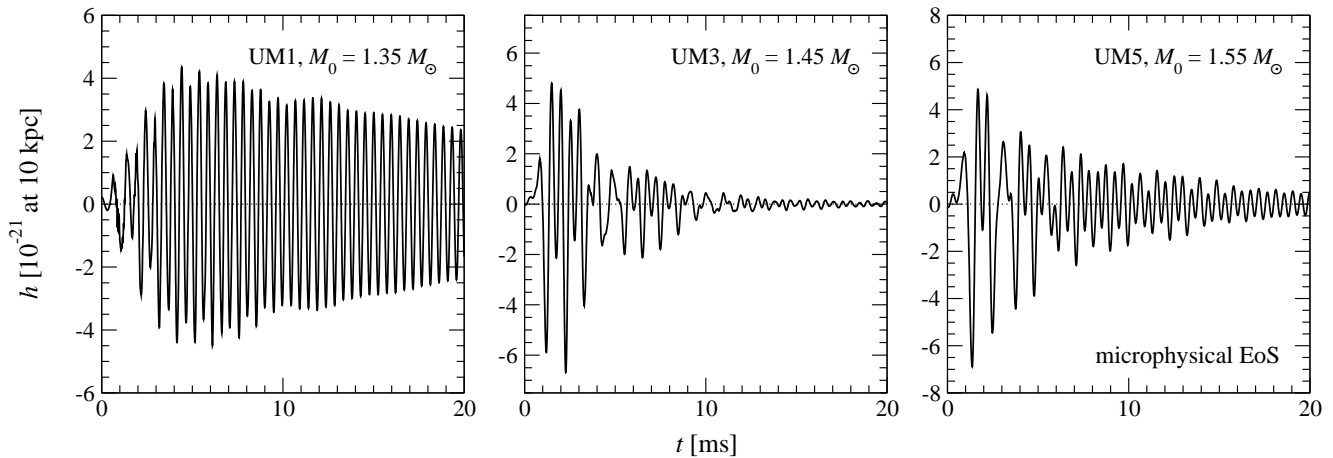


**Figure 13.** Time evolution of the gravitational wave strain  $h$  for three migration models of family UM with the microphysical EoS.

energy. Furthermore, rapid rotation also causes the regular fundamental quasi-radial  $F$ -mode to acquire such a strong quadrupolar nature that it becomes the main gravitational wave emitting mode, surpassing the  ${}^2f$ -mode in peak height in the waveform spectrum (see also the discussion in Section 4.5). Therefore, even if for such models the  ${}^2f$ -mode was somewhat amplified, this would not be identifiable in the spectrum, which is dominated by the  $F$ -mode. We also note that the inefficacy of this type of mode resonance for rapid rotation was also found by Abdikamalov et al. (2009) in their simulations of the collapse of neutron star models to hybrid quark stars.

We also note that although in the dynamic collapse phase of a migration the self-couplings of the  $F$ -mode, which are responsible for transferring energy into the emitting  ${}^2f$ -mode, are much more violently excited, they are also present in perturbed equilibrium models. Consequently, we observe the effects of mode resonance not only in some of the migrating models of family US and UM, but also in the corresponding equilibrium models of family PMS and PMM, if these are subjected to a small amplitude initial perturbation according to Eq. (19), which favors the excitation of quasi-radial  $l = 0$  modes. As expected, the quadrupolar  $l = 2$  perturbation of Eq. (20) excites self-couplings of the

$F$ -mode only weakly, and thus in that case mode resonance does not occur in any of the equilibrium models.

#### 4.5 Detectability prospects of gravitational waves

Due to the long quasi-periodic emission time the gravitational waves emitted by a migration event is a promising source for gravitational wave detectors of both interferometer or resonant type. Assuming that the strong post-collapse oscillations are not damped by any other physical mechanism than dissipation of kinetic energy by shocks, the damping we observe for the models of family US suggests that the effective total emission time for gravitational waves can be much longer than the evolution time of our models (which is  $t_f = 50$  ms), i.e. last for hundreds of pulsation cycles. In contrast, the models of family UM are so strongly damped that the emission of gravitational waves has essentially died out at the end of the evolution time at  $t = 50$  ms.

To assess the prospects for detection by current and planned interferometric detectors, we calculate characteristic quantities for the gravitational wave signal following Thorne (1987). Applying a Fourier transform to the dimensionless gravitational wave strain  $h$ , we obtain

**Table 6.** Detection prospects for gravitational waves.  $f_c$  is the characteristic frequency,  $h_c$  is the integrated characteristic gravitational wave signal strain and SNR is the signal-to-noise ratio, each given for the LIGO detector, the VIRGO detector, and the Advanced LIGO detector in broadband mode. All quantities assume a total emission time of  $t_f = 50$  ms and are dependent on the rms strain noise  $h_{\text{rms}}$  of the detector.

Model	$f_{c,\text{LIGO}}$ [kHz]	$f_{c,\text{VIRGO}}$ [kHz]	$f_{c,\text{Adv. LIGO}}$ [kHz]	$h_{c,\text{LIGO}}$ $\left[10^{-21}\right]$ [at 10 kpc]	$h_{c,\text{VIRGO}}$ $\left[10^{-21}\right]$ [at 10 kpc]	$h_{c,\text{Adv. LIGO}}$ $\left[10^{-21}\right]$ [at 10 kpc]	SNR <sub>LIGO</sub> [at 10 kpc]	SNR <sub>VIRGO</sub> [at 10 kpc]	SNR <sub>Adv. LIGO</sub> [at 10 kpc]
US1	1.768	1.786	1.798	2.6	2.6	2.6	0.3	0.5	9.2
US2	1.225	1.321	1.432	10.4	11.0	11.7	2.1	3.4	54.9
US3	1.574	1.651	1.728	31.6	32.9	34.1	4.4	7.6	127.6
US4	0.924	1.006	1.129	9.3	9.8	10.7	2.9	4.4	65.0
US5	0.718	0.766	0.834	5.8	6.0	6.4	2.6	3.7	51.8
UM1	2.024	2.031	2.041	18.6	18.7	18.7	1.8	3.2	56.6
UM2	1.928	1.952	1.983	22.0	22.2	22.5	2.3	4.0	70.6
UM3	1.236	1.297	1.384	7.0	7.2	7.6	1.4	2.3	37.0
UM4	1.130	1.190	1.282	7.9	8.2	8.6	1.8	2.9	45.7
UM5	1.047	1.110	1.202	7.5	7.8	8.3	1.9	3.1	47.3
UM6	1.007	1.078	1.178	8.8	9.2	9.8	2.4	3.8	57.3

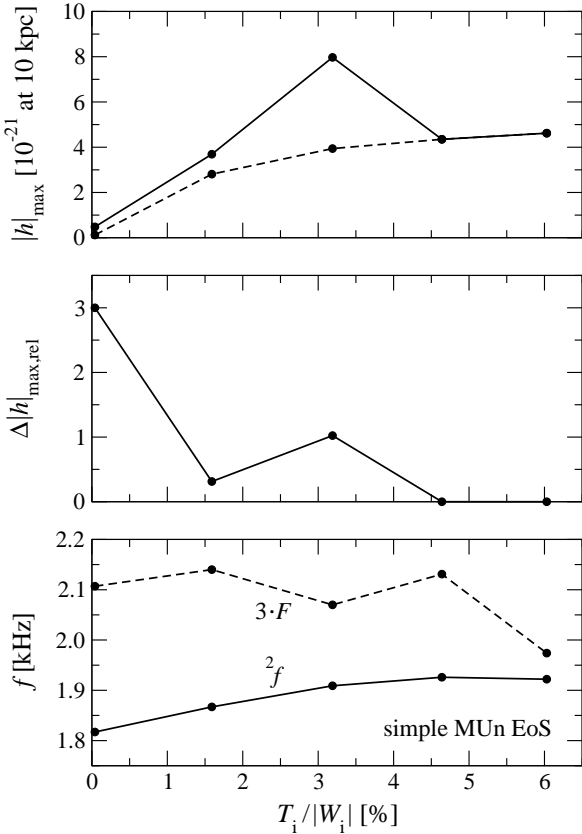


**Figure 14.** Dependence of the maximum gravitational wave strain  $|h|_{\text{max}}$  (top panel), the relative amplification of the maximum gravitational wave strain  $\Delta|h|_{\text{max,rel}}$  (center panel), and the frequency  $f$  for potentially resonating modes (bottom panel) on the initial rotation rate  $T_i/|W_i|$  for the migration models of family US with the simple MUn EoS.  $|h|_{\text{max}}$  is given with (solid line) and without (dashed line) taking into account the effects of mode resonance, and  $\Delta|h|_{\text{max,rel}}$  is the relative increase in  $|h|_{\text{max}}$  due to mode resonance. The frequencies of the  $2f$ -mode and  $3 \cdot F$ -mode are marked with a solid and dashed line, respectively.

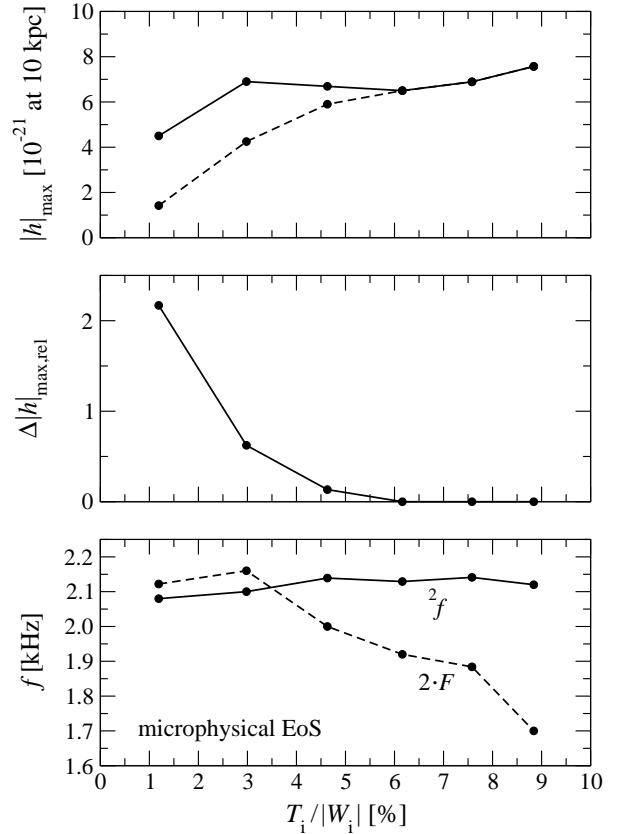


**Figure 15.** Dependence of the maximum gravitational wave strain  $|h|_{\text{max}}$  (top panel), the relative amplification of the maximum gravitational wave strain  $\Delta|h|_{\text{max,rel}}$  (center panel), and the frequency  $f$  for potentially resonating modes (bottom panel) on the initial rotation rate  $T_i/|W_i|$  for the migration models of family UM with the microphysical EoS.  $|h|_{\text{max}}$  is given with (solid line) and without (dashed line) taking into account the effects of mode resonance, and  $\Delta|h|_{\text{max,rel}}$  is the relative increase in  $|h|_{\text{max}}$  due to mode resonance. The frequencies of the  $2f$ -mode and  $2 \cdot F$ -mode are marked with a solid and dashed line, respectively.



$$\hat{h} = \int_{-\infty}^{\infty} e^{2\pi i f t} h dt. \quad (21)$$

One can compute the (detector dependent) integrated characteristic frequency as

$$f_c = \left( \int_0^{\infty} \frac{\langle \hat{h}^2 \rangle}{S_h} f df \right) \left( \int_0^{\infty} \frac{\langle \hat{h}^2 \rangle}{S_h} df \right)^{-1}, \quad (22)$$

and the dimensionless integrated characteristic strain as

$$h_c = \left( 3 \int_0^{\infty} \frac{S_{h_c}}{S_h} \langle \hat{h}^2 \rangle f df \right)^{1/2}, \quad (23)$$

where  $S_h$  is the power spectral density of the detector and  $S_{h_c} = S_h(f_c)$ . We approximate the average  $\langle \hat{h}^2 \rangle$  over randomly distributed angles by  $\hat{h}^2$ , assuming optimal orientation of the detector. From Eqs. (22, 23) the signal-to-noise ratio can be calculated as  $\text{SNR} = h_c/[h_{\text{rms}}(f_c)]$ , where  $h_{\text{rms}} = \sqrt{f S_h}$  is the value of the rms strain noise for the detector (which gives the theoretical sensitivity window). In Table 6 we summarize the values of  $f_c$ ,  $h_c$  and the signal-to-noise ratio for all the migrating models of the two families US and UM for the currently operating LIGO and VIRGO detectors and for the future Advanced LIGO detector in broad band operation mode<sup>9</sup>. Here we consider a source inside our own Galaxy at a reference distance of 10 kpc.

The fraction of neutron stars that undergo a migration process at some stage in their lifetimes is rather uncertain. In this work we restrict ourselves to considering isolated neutron stars. Depending on the selected gravitational mass and the EoS, such a neutron star must have spun down to somewhere between 50 and 800 Hz to be subject to a migration (see Table 1, and Figs. 2 and 3), provided it has an EoS that is similar to one of our choice and shows the back bending phenomenon.

Apparently, isolated millisecond pulsars with low magnetic field, which have been recycled by accretion, are no appropriate candidates, as they spin down too slowly, on a Hubble time scale. However, there exists another class of neutron stars, which are thought to rotate initially at a millisecond period, and those are magnetars. In order to generate the required surface magnetic field of roughly  $10^{14}$  to  $10^{15}$  G, the proto-neutron star born in a type II supernova explosion must rotate at  $\sim 500$  Hz. Due to strong magnetic breaking, it slows down to a few Hz after only about  $10^3$  y.

The most dramatic spin-down of a magnetar occurs during the first years of its life, which is the period when the migration phenomenon could occur. So far ten magnetars were detected in Galaxy: six anomalous X-ray pulsars and four soft-gamma repeaters. Magnetars are active and therefore observable for about  $10^3 - 10^4$  y. This means that their birth rate is not much smaller than that of ‘‘ordinary’’ radio pulsars (with a lifetime of  $\sim 10^6$  y), which in turn is comparable to the type II supernova rate in a big spiral galaxy like ours. Consequently, we may expect about one migration event in our Galaxy per century, which is a very low rate. Consistent

with this simple argument, an analysis based on observational data yields a very uncertain birth rate between 0.2 and 6 per century (Muno et al. 2007; Gill & Heyl 2007). The magnetar birth rate rises to about one per year if the whole Virgo cluster of galaxies is considered (Dall’Osso & Stella 2007).

Still, if such a migration event did occur in our Galaxy, for current interferometric detectors of the LIGO class and assuming an emission time  $t_f = 50$  ms, all of our models except the slowly rotating one US1 have a signal-to-noise ratio very close to or above 1. Model US3, which is both moderately rapidly rotating and whose gravitational wave emission is amplified by mode resonance (see center panel of Fig. 12), features the largest signal-to-noise ratio of all investigated models at about 4 for current LIGO and 8 for current VIRGO. For the Advanced LIGO detector, the signal-to-noise ratio lies comfortably above 10 for all models (again except model US1 which still yields  $\text{SNR} = 9$ ) and reaches  $\sim 130$  in model US3. It is remarkable that  $h_c$  (and correspondingly, also the signal-to-noise ratio) for the model family UM with the microphysical EoS is bounded by a rather narrow interval between about 7 and  $22 \times 10^{-21}$  at 10 kpc, although the initial rotation rates of the models span a wide range (see Table 1).

For substantially increasing the event rate, it would be necessary for the detector to be sensitive to signals coming from distances out to the Virgo cluster, at  $\sim 20$  Mpc. However, at this distance the signal-to-noise ratios for our models given in Table 6 must to be scaled down by a factor of 2000 and consequently drop to well below 1 even for Advanced LIGO. Therefore, as for gravitational wave signals from supernova core collapse (see the discussion in Dimmelmeier et al. 2007), the second generation detectors will improve the signal-to-noise ratio of a local event alone, but will not increase the event rate much on account of the inhomogeneous galaxy distribution in the local region of the Universe. Only third generation detectors will have the required sensitivity in the kHz range to achieve a robust signal-to-noise ratio at the distance of the Virgo cluster.

Note that for most of the models the *integrated* characteristic frequency  $f_c$  given in Table 6 is not very close to either of the two main gravitational wave emission frequencies  $f_F$  and  $f_{2f}$ . This is because  $f_c$  reflects the frequency dependence of the sensitivity of the detector, because nonlinear mode couplings and higher-order linear modes also contribute to the gravitational wave signal (although with lower relative amplitudes) and, most importantly, because for many models the gravitational wave power spectrum of the signal exhibits two strong peaks from the  $F$ -mode and the  $2f$ -mode. Based on the peak height in the spectrum of the gravitational radiation waveform, we find that the fundamental quadrupolar  $2f$ -mode is the strongest emitter for the slowly and moderately rapidly rotating models, followed by the fundamental quasi-radial  $F$ -mode. For rapid rotation, this order of importance is reversed.

The detector dependence of  $f_c$  and  $h_c$  is also illustrated in Fig. 16, where the locations of the gravitational wave signals for all models are plotted relative to the rms strain noise  $h_{\text{rms}}$  of the current LIGO and VIRGO detectors (left and center panels, respectively) and the future Advanced LIGO detector (right panel), all for a distance to the source of 10 kpc. Model US3, which both has significant rotation and

<sup>9</sup> Note that both in Table 6 and in Fig. 16 the gravitational wave characteristics have been evaluated for a total emission time of  $t_f = 50$  ms, where the waveform amplitude of at least the models of family US has not yet decayed to zero. Therefore, for these models the values for  $h_c$  and the signal-to-noise ratio shown here are actually a lower bound.

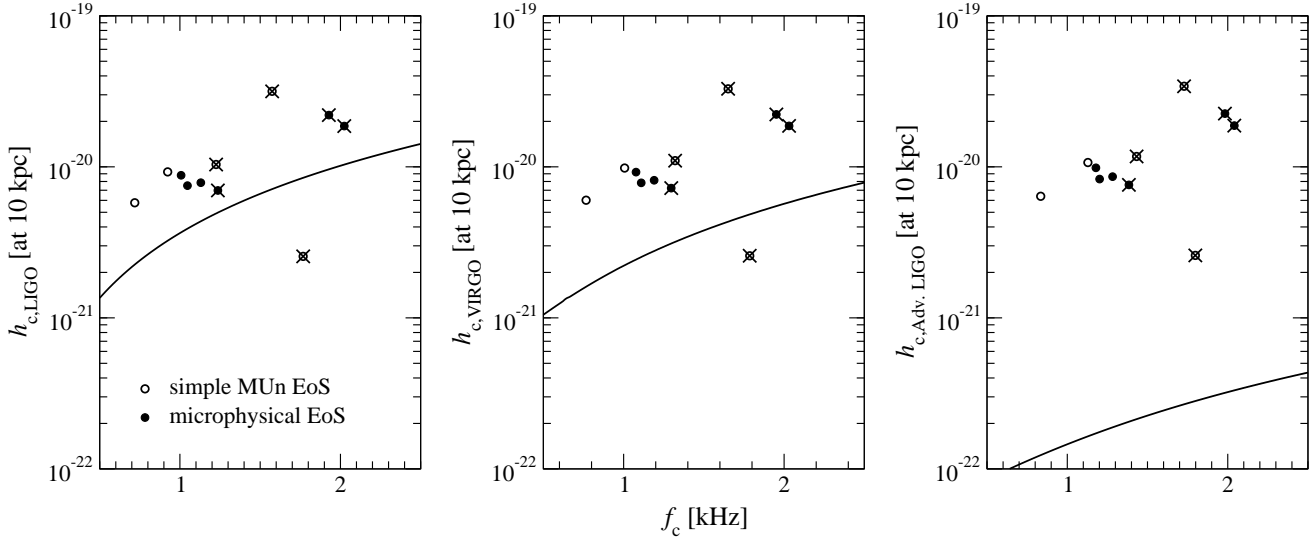


**Figure 16.** Location of the gravitational wave signals for the migration models from family US with the simple MUn EoS (filled circles) and family UM with the microphysical EoS (open circles) in the  $h_c$ - $f_c$  plane relative to the sensitivity curves (i.e. the rms strain noise  $h_{\text{rms}}$ ) of the LIGO detector (left panel), VIRGO detector (center panel), and Advanced LIGO detector in broadband mode (right panel), all at a distance of 10 kpc. Models whose gravitational wave emission is amplified by mode resonance effects are marked with a cross.

exhibits mode resonance (models where more resonance amplifies gravitational radiation emission are marked by crosses in Fig. 16), clearly sticks out with the largest values of  $h_c$ . In general, models with initially moderate rotation, whose waveform amplitudes are in addition boosted by mode resonance effects, are found in the upper right quarter of the diagram, i.e. they feature both a high characteristic frequency and a large characteristic strain. Model US1, which is by far the slowest rotator, shows the smallest value for  $h_c$ , albeit at a comparably high  $f_c$ .

From Fig. 16 it is clear that a possible detection is hampered by the adverse characteristics of the detector sensitivity curve in the frequency interval relevant for our models, where the strain noise  $h_{\text{rms}}$  rises steeply with frequency. Proposed future detectors with a flat  $h_{\text{rms}}$  curve up to frequencies in the kHz range could eliminate this problem.

Interestingly, if a larger selection of models that are evenly distributed in the parameter space of initial rotation rate were simulated, their distribution in the  $h_c$ - $f_c$  plane would most probably very well approximate the pattern found by Dimmelmeier et al. (2008) for rotating models of collapsing stellar cores in a supernova event. In order to filter out the effects of mode resonance, which for some models amplifies the waveform amplitude in the ring-down following the collapse phase and which cannot be simply subtracted from the time integrated characteristic strain  $h_c$ , in Fig. 17 instead of  $h_c$  we plot the maximum gravitational wave strain  $|h|_{\text{max}}$  around the time of maximum compression (i.e. the most dynamic moment of the collapse phase) before any possible waveform amplification by mode resonance.

As for  $h_c$  in Fig. 17 of Dimmelmeier et al. (2008), starting from very slowly rotating models  $|h|_{\text{max}}$  and (not as strongly)  $f_c$  increase as rotation grows (see arrow 1 in their figure and our Fig. 17), then only the waveform amplitude rises at practically constant  $f_c$  (arrow 2 again in both figures). We recall that for these models the  $^2f$ -mode is the strongest emitter, which depends

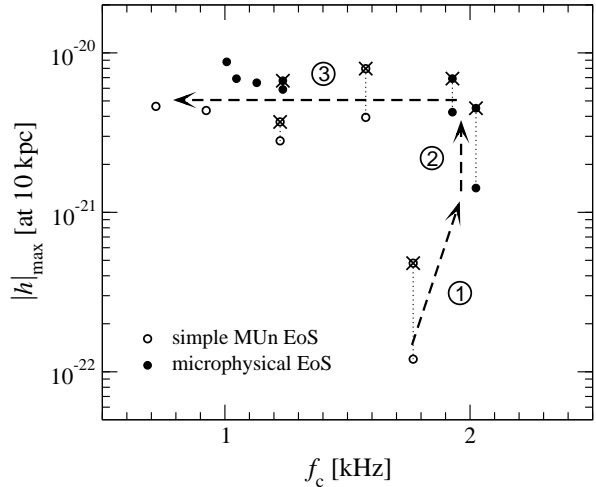


**Figure 17.** Dependence of the maximum gravitational wave strain  $|h|_{\text{max}}$  on the characteristic frequency  $f_c$  for the migration models of family US with the simple MUn EoS (unfilled circles) and family UM with the microphysical EoS (filled circles). If mode resonance influences gravitational wave emission (models denoted with a cross),  $|h|_{\text{max}}$  also is computed around the time of maximum compression before the amplification of  $h$  takes effect. The decrease of  $|h|_{\text{max}}$  without resonance effects is marked by dotted lines. The arrows indicate the qualitative effect of increasing initial rotation rate  $T_i/|W_i|$ .

only weakly on rotation (see Tables 4 and 5, and also Dimmelmeier, Stergioulas & Font 2006), which explains the approximate constancy of  $f_c$  in this regime. This weak imprint of rotation is in stark contrast to e.g. a rigidly rotating bar, where the emission frequency increased linearly with rotation frequency.

Finally, for rapidly rotating models which run into the centrifugal barrier,  $|h|_{\text{max}}$  saturates at a constant or even slightly declining level with significantly decreasing fre-

quency  $f_c$  (arrow 3 again in both figures). What we do not observe here is the rather separate group of extremely rotating models, whose evolution and waveforms are dominated by centrifugal forces (marked by 4 in their figure). In addition, in our case mode resonance effects would bulge out the “knee” for moderately rotating models in the upper right corner of the curve towards higher values of  $h_c$  (or in our case  $|h|_{\max}$ ), as seen in Fig. 17, where for such models the maximum amplitude for the *entire* waveform (marked by crosses) is higher than if only taken in the period around maximum compression.

## 5 SUMMARY AND CONCLUSIONS

We have studied the mini-collapse of rotating neutron star models induced by a dynamic back bending instability. This instability is caused by the softening of the equation of state resulting from a phase transition in the dense core. The collapse leads to a migration of the neutron star from an unstable equilibrium configuration to a stable one after a series of damped pulsations. The migration starts when the configuration reaches the local minimum of the total angular momentum in the back bending diagram. We have investigated two families of models, one with the simple analytic MUn equation of state and one with a tabulated microphysical equation of state that includes effects of a phase transition due to kaon condensation.

If the rotation profile of the neutron star remained uniform during the collapse, the neutron star would simply migrate horizontally (i.e. at constant total angular momentum) from the unstable branch to the stable branch (which are separated by the unstable segment) in the angular momentum vs. rotation frequency diagram. However, our simulations show that the neutron star actually develops a differential rotation profile. Still, we find that the final degree of differential rotation is not large and that the new equilibrium configuration is similar to the corresponding one on the stable branch in the back bending diagram under the assumption of rigid rotation.

The dynamic collapse in the migration process creates a whole spectrum of coupled pulsation modes, which we extract directly from the numerical results of our fully nonlinear simulations. In addition, we have also constructed equilibrium models which closely resemble the post-migration configurations, and evolved them after applying a small perturbation. Using both approaches, we have identified the characteristics of the main modes excited by the mini-collapse, and find evidence for resonance between the fundamental quadrupolar mode and nonlinear self-couplings of the fundamental quasi-radial mode. Our results show that the amplitude and waveform of gravitational radiation depends strongly on the mass of the star and the equation of state used. Namely, models with the microphysical of state, which features a density jump associated with a first-order phase transition, suffer from much stronger damping than models with the mixed-phase MUn equation of state.

In the case of a detection with current or future gravitational wave interferometer detectors (like VIRGO or LIGO), such imprints of the model parameters on the waveform properties could be exploited to observationally constrain the unknown equation of state for dense matter. For a Galac-

tic event, whose frequency of occurrence should be comparable with the local type II supernova rate, the predicted gravitational wave signal from such a dynamic migration lies above the designed sensitivity curves of current km-size detectors. With future, more sensitive detectors, signals from events within the Virgo cluster of galaxies could also come into range. Then the corresponding event rate could possibly increase to about one per year. In addition, we find that in some cases the gravitational wave emission is considerably enhanced due to the said mode resonance, which transfers energy from the strongly excited but weakly radiating quasi-radial mode to the initially weakly excited but strongly radiating quadrupolar mode.

Particularly promising candidates for a dynamic migration are young magnetars, as they have an initial rotation rate in the kHz range and spin down very rapidly. While the prospective astrophysical phenomenon we study in this work seems to be rare, it has nevertheless a potential of producing a very characteristic signature in the form of a peculiar burst of gravitational radiation. The damping of the post-migration pulsations, which is directly reflected in the gravitational wave signal, is even sensitive to the character of the phase transition softening, i.e. whether it occurs with or without a jump in density. Therefore, if chance allows us to detect such a dynamic migration event in our Galaxy, this will possibly be a source of rich information about the structure of the superdense neutron star core.

We point out that in our simulations the effects of the magnetic field, which for magnetars has a typical strength of  $B \sim 10^{14} - 10^{15}$  G, are neglected. In particular the impact on the stellar shape is discarded. However, the typical pressure in neutron star cores, where the phase transition in the equation of state that causes the back bending phenomenon occurs, is  $10^{34} - 10^{35}$  dyn cm<sup>-2</sup> (see Figure 1), while with  $B^2/(8\pi) \sim 4 \times 10^{29} (B/10^{15} \text{ G})^2$  the stress due to the magnetic field is many orders of magnitude lower. Therefore, the influence of even a strong magnetic field on the core structure is small, and consequently we expect only secondary effects on the back bending instability.

We close by pointing out that the results presented here should be considered as a first step towards a better understanding of the neutron star interior and dynamical phenomena like migration from unstable to stable configurations. Due to the presently very limited knowledge about the equation of state for dense matter, some of the aspects of the physical processes underlying the investigated scenario are necessarily simplified. The treatment of the equation of state as a representation of matter in the mixed phase experiencing a phase transition is rather crude, especially when one considers the behavior of fluid elements undergoing successive stages of compression and decompression, and changing the proportions of the phases. In particular, our modeling neglects any possible effects from local heating, or from the creation and subsequent emission of neutrinos during the migration collapse and the subsequent bounces. On the other hand we have shown that the time scale of the mini-collapse is short enough to neglect non-equilibrium and bulk viscosity effects.

**ACKNOWLEDGMENTS**

It is a pleasure to thank Jérôme Novak, Christian D. Ott and Nikolaos Stergioulas for helpful comments and discussions. Part of this work was done during a visit of H.D. at the Nicolaus Copernicus Astronomical Center in Warsaw, Poland. He expresses his gratitude for the hospitality of the host group. H.D. acknowledges a Marie Curie Intra-European Fellowship within the 6th European Community Framework Programme (IEF 040464), and M.B. acknowledges Marie Curie Fellowships within the 6th and 7th European Community Framework Programmes (MEIF-CT-2005-023644 and ERG-2007-224793). This work was supported by the DAAD and IKY (IKYDA German–Greek research travel grant) and by the Polish MNiSW grant no. N20300632/0450.

**REFERENCES**

- Abdikamalov E. B., Dimmelmeier H., Rezzolla L., Miller J., 2009, *Mon. Not. R. Astron. Soc.*, accepted; [www.arxiv.org/abs/0806.1700](http://www.arxiv.org/abs/0806.1700)
- Arnowitt R., Deser S., Misner C. W., 1962, in Witten L., ed, *Gravitation: An introduction to current research*. Wiley, New York, USA
- Banyuls F., Font J. A., Ibáñez J. M., Martí J. M., Miralles J. A., 1997, *ApJ*, 476, 221
- Baym G., Pethick C. J., Sutherland P., 1971, *ApJ*, 170, 299
- Bisnovatyi-Kogan G. S., Seidov E. F., 1984, *Astrofiz.*, 21, 563
- Chatterjee D., Bandyopadhyay D., 2007, *Phys. Rev. C*, 75, 123006
- Cordero-Carrión I., Cerdá-Durán P., Dimmelmeier H., Jaramillo J. L., Novak J., Gourgoulhon E., 2009, *Phys. Rev. D*, submitted; [www.arxiv.org/abs/0809.2325](http://www.arxiv.org/abs/0809.2325)
- Dall’Osso S., Stella L., 2007, *Ap&SS*, 308, 119
- Dimmelmeier H., Cerdá-Durán P., Marek A., Faye G., 2006, in Alimi J.-M., Füzfa A., eds, *Proc. Albert Einstein’s Century International Conference*, Paris, France, 2005. AIP Conference Proceedings, AIP Publishing, Melville, astro-ph/0603760
- Dimmelmeier H., Font J. A., Müller E., 2002a, *A&A*, 388, 917
- Dimmelmeier H., Font J. A., Müller E., 2002b, *A&A*, 393, 523
- Dimmelmeier H., Novak J., Font J. A., Ibáñez J. M., Müller E., 2005, *Phys. Rev. D*, 71, 064023
- Dimmelmeier H., Ott C. D., Janka H.-T., Marek A., Müller E., 2007, *Phys. Rev. Lett.*, 98, 251101
- Dimmelmeier H., Ott C. D., Marek A., Janka H.-T., 2008, *Phys. Rev. D*, 78, 064056
- Dimmelmeier H., Stergioulas N., Font J. A., 2006, *MNRAS*, 368, 1609
- Donat R., Font J. A., Ibáñez J. M., Marquina A., 1996, *J. Comput. Phys.*, 146, 58
- Douchin F., Haensel P., 2001, *A&A*, 380, 151
- Eardley D. M., 1983, in Deruelle N., Piran T., eds, *Gravitational Radiation*, Proc. Advanced Study Institute, Les Houches, France. North-Holland Publishing Company, Amsterdam
- Font J. A., Goodale T., Iyer S., Miller M., Rezzolla L., Seidel E., Stergioulas N., Suen W.-M., Tobias M., 2002, *Phys. Rev. D*, 65, 084024
- Gill R., Heyl J., 2007, *MNRAS*, 381, 52
- Glendenning N. K., Pei S., Weber F., 1997, *Phys. Rev. Lett.*, 79, 1603
- Glendenning N. K., Schaffner-Bielich J., 1999, *Phys. Rev. C*, 60, 025803
- Glendenning N. K., 2000, *Compact Stars, Nuclear Physics, Particle Physics and General Relativity*. Springer, New York
- Gourgoulhon E., Haensel P., Gondek D., 1995, *A&A*, 294, 747
- Haensel P., Levenfish K. P., Yakovlev D. G., 2002, *A&A*, 394, 213
- Haensel P., Pichon B., 2001, *A&A*, 283, 313
- Haensel P., Potekhin A.Y., Yakovlev D.G., 2007, *Neutron Stars I. Equation of State and Structure*. Springer, New York
- Haensel P., Zdunik J. L., Schaeffer R., 1989, *A&A*, 217, 139
- Isenberg J. A., 2008, *Int. J. Mod. Phys. D*, 17, 265
- Komatsu H., Eriguchi Y., Hachisu I., 1989, *MNRAS*, 237, 355
- Lin L. M., Gheng K. S., Chu M. C., Suen W.-M., 2006, *A&A*, 639, 382
- Madsen J., 1999, in Cleymans J., ed, *Hadrons in Dense Matter and Hadrosynthesis*. Springer, Berlin, p. 162
- Muno M. P., Gaensler B. M., Nechita A., Miller J. M., Slane P.O., 2007, *ApJ*, 680, 639
- Nagar A., Zanotti O., Font J. A., Rezzolla L., 2007 *Phys. Rev. D*, 75, 044016
- Ott C. D., Dimmelmeier H., Marek A., Janka H.-T., Zink B., Hawke I., Schnetter E., 2007, *Class. Quantum Grav.*, 24, S139
- Saijo M., 2004, *APJ*, 615, 866
- Shibata M., Sekiguchi Y.-I., 2003, *Phys. Rev. D*, 68, 104020
- Shibata M., Sekiguchi Y.-I., 2004, *Phys. Rev. D*, 69, 084024
- Stergioulas N., Friedman J. L., 1995, *APJ*, 444, 306
- Thorne K. S., 1987, in Hawking S. W. and Israel W., ed, 300 *Years of Gravitation*. Cambridge University Press, Cambridge
- Thorne K. S., 1980, *Rev. Mod. Phys.*, 52, 299
- Weber F., *Pulsars as Astrophysical Laboratories for Nuclear and Particle Physics*. IOP Publishing, Bristol
- Wilson J. R., Mathews J. R., Marronetti P., 1996, *Phys. Rev. D*, 54, 1317
- Zdunik J. L., 2000, *A&A*, 359, 311
- Zdunik J. L., Bejger M., Haensel P., Gourgoulhon E., 2006, *A&A*, 450, 747
- Zimanyi J., Moszkowski S. A., 1990, *Phys. Rev. C*, 42, 1416

**APPENDIX A: NON-EQUILIBRIUM EFFECTS IN THE EQUATIONS OF STATE**

In its quasi-stationary evolution phase, the rotating neutron star slowly proceeds along the stable branch. Here the slow angular momentum loss results in an according compression of the neutron star matter. When it enters the dynamic migration period, the phase transition in the stellar core leads to a much more rapid initial contraction, followed by several re-expansion and compression cycles (see Figs. 6 and 7). In both regimes the composition of matter has to re-adjust to the change in density and pressure to keep matter in thermodynamic equilibrium. This process of equilibration of com-



position proceeds via nuclear reactions, of which the ones involving weak interaction (changing lepton number and/or strangeness per baryon) are the slowest. We now investigate these relaxation processes and their impact on the EoS of compressed matter separately for the two regimes.

When the neutron star evolves on the stable branch (marked by solid lines in Figs. 2 and 3), it moves slowly downwards along the branch on a characteristic secular time scale  $\tau_{\text{sec}} = \rho_c / \dot{\rho}_c \propto (J/|\dot{J}|)^{-1}$ . This time scale is so long that equilibration nearly catches up with compression, and any deviations from equilibrium are tiny. Consequently, the EoS of matter can be well approximated by assuming full equilibrium.

As soon as the marginally stably equilibrium configuration is reached, further loss of  $J$  triggers the dynamic migration, associated with a compression of matter on the dynamic time scale  $\tau_{\text{dyn}} \lesssim 1$  ms. Now matter moves off weak equilibrium and the actual EoS stiffens compared to the fully equilibrated one (see e.g. Gourgoulhon, Haensel & Gondek 1995; Haensel, Levenfish & Yakovlev 2002, and references therein). However, a deviation from equilibrium accelerates (in a strongly nonlinear manner) the rate of equilibration processes, which tend to return the matter towards equilibrium following le Châtelier's principle. Consequently, also in the migration phase (i.e. the rapid initial contraction and the subsequent pulsations) the EoS is quite close to the equilibrium one. Strictly speaking, the deviation from equilibrium is such that as to make the rate of equilibration equal to the time scale of dynamic compression. Still, the effect on the dynamics is small, and is thus being neglected in our calculation.

## APPENDIX B: PULSATION DAMPING IN THE MICROPHYSICAL EQUATION OF STATE

The damping of the post-migration pulsations observed in the models of family UM with the microphysical EoS is much stronger than in family US with the simple MUn EoS (cf. Figs. 7 and 6, respectively). It is caused by a particular, very efficient damping mechanism that occurs if matter moves across a first-order phase transition in such a type of EoS due to quasi-radial pulsations (Bisnovatyi-Kogan & Seidov 1984; Haensel, Zdunik & Schaeffer 1989). In the following, we explain that mechanism and the relevant energy and time scales in our models in more detail. For simplicity, without loss of generality we do not take into account effects of rotation and only consider spherically symmetric Newtonian models.

### B1 Radial pulsations of the dense core

First we consider a rather simplified model of a pulsating compact star with an EoS that exhibits a phase transition and leads to a dense core in the center of the star. We neglect finite compressibility of matter outside the core (except for the phase transition), so that the star's density there is simply  $\rho_1$ .

Conservation of mass then leads to a relation between the pulsation amplitude  $\delta r_c$  of the dense core radius and the radial velocity  $v_{r>r_c}$  of the pulsations outside the core,

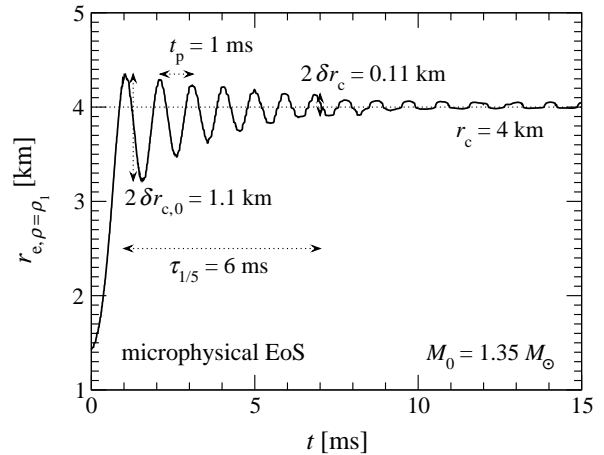


**Figure B1.** Time evolution of the radius  $r_{e,\rho=\rho_1}$  of the dense core in the equatorial plane for the slowest rotating model UM1 of family UM with the microphysical EoS. The pulsation period of  $r_{e,\rho=\rho_1}$  is roughly  $t_p = 1$  ms. The pulsation amplitude  $\delta r_c$  is damped to 1/5 of its initial value of about  $\delta r_{c,0} = 0.55$  km in approximately  $\tau_{1/5} = 6$  ms. The equatorial radius of the dense core finally settles at the equilibrium value  $r_c = 4$  km.

$$v_{r>r_c} = \omega \delta r_c \left( \frac{r_c}{r} \right)^2 (\lambda - 1), \quad (\text{B1})$$

where  $r_c$  is the unperturbed equilibrium radius of the dense core,  $r$  is the unperturbed radial coordinate,  $\omega$  is the angular pulsation frequency, and  $\lambda = \rho_2/\rho_1$  quantifies the jump in density at the core edge due to the phase transition in the EoS. The phases of  $\delta r_c(t)$  and  $v_{r>r_c}(t)$  differ by  $\pi$ . As the core matter is incompressible, the velocity  $v_{r<r_c}$  at radii smaller than  $r_c$  vanishes.

Under our simple model assumptions, the average kinetic energy contained in the radial pulsations is then given by

$$\begin{aligned} \bar{E}_p &= \pi \int_{r_c}^{r_s} dr r^2 \rho_1 v_{r>r_c}^2 \\ &= \pi \rho_1 r_c^3 \omega^2 (\lambda - 1)^2 \left( 1 - \frac{r_c}{r_s} \right) (\delta r_c)^2, \end{aligned} \quad (\text{B2})$$

where  $r_s$  is the unperturbed equilibrium radius of the star.

The stable equilibrium initial model PMM1 that corresponds to the post-migration state of model UM1 has a stellar radius  $r_{s,0} \approx 12$  km, while from Fig. B1 we can extract typical values  $\delta r_{c,0} \approx 0.55$  km and  $r_{c,0} \approx 4$  km at the start of the post-migration pulsations<sup>10</sup>. For our microphysical EoS the density discontinuity corresponds to  $\lambda = 1.62$  (see Section 3.1 and Fig. 1). Thus, from Eq. (B2) we obtain for the initial pulsation energy:

$$\bar{E}_{p,0} \approx 3.7 \times 10^{48} \text{ erg}. \quad (\text{B3})$$

<sup>10</sup> For the other models of family UM we obtain similar values for  $\delta r_{c,0}$  and  $r_{c,0}$  and  $r_{s,0}$ . In Fig. B1 we show the evolution of  $r_{\rho=\rho_1}$  only in the equatorial plane, as both the qualitative behavior and the typical scale of this quantity does not depend much on latitude.

## B2 Dissipation from a first-order phase transition and associated damping time scale

We now consider the situation where the matter on both sides of  $r_c$  is fully equilibrated, i.e. realizes a minimum of the appropriate thermodynamic potential (Bisnovatyi-Kogan & Seidov 1984). The kinetic energy associated to the pulsations is dissipated during the first-order phase transition, as matter passes through the boundary of the dense core<sup>11</sup>. Actually, the dissipation occurs during the compression phase, which is the first half of the pulsation period  $t_p$ , and takes place within the shock front that forms at the dense core edge. In the thin layer between the two phases, the sound speed  $c_s \approx [(P_2 - P_1)/(\mathcal{E}_2 - \mathcal{E}_1)]^{1/2}$  is rather low, because the large density jump is associated with only a very small pressure increase. Therefore the matter flow within this layer is supersonic. In reality, the dissipation within the shock heats up the matter that flows into the dense core. However, in our approximation we neglect thermal effects in the EoS, and thus dissipation manifests itself only via the loss of kinetic energy in the matter flow<sup>12</sup>.

The average energy dissipated during one oscillation period is (Bisnovatyi-Kogan & Seidov 1984)

$$\bar{E}_{d,t_p} = \frac{4\pi}{3} r_c^2 \left( \frac{2\pi}{t_p} \right)^2 \rho_1 \lambda(\lambda - 1) (\delta r_c)^3. \quad (\text{B4})$$

This dissipation results in a damping of pulsations and the decrease of  $\delta r_c$ .

Assuming that all terms in Eq. (B4) except  $\delta r_c$  are constant, we obtain for the average dissipated power

$$\dot{\bar{E}}_d = \bar{E}_{d,t_p} / t_p = \dot{\bar{E}}_{d,0} \left( \frac{\delta r_c}{\delta r_{c,0}} \right)^3. \quad (\text{B5})$$

Evaluating Eq. (B4) at the initial pulsation time and using the approximate value  $t_p \approx 1$  ms extracted from Fig. B1 together with the other estimates from Appendix B1 and  $\rho_1$  for the microphysical EoS, the power dissipated during the first pulsation period is

$$\dot{\bar{E}}_{d,0} \approx 3 \times 10^{48} \text{ erg ms}^{-1}. \quad (\text{B6})$$

We now demand that the change in pulsation energy is entirely caused by the above dissipation mechanism, and thus we arrive at

$$\frac{d\bar{E}_p}{dt} = -\dot{\bar{E}}_d. \quad (\text{B7})$$

Rewriting Eq. (B2) for the average kinetic energy associated to the pulsations as

$$\bar{E}_p = \bar{E}_{p,0} \left( \frac{\delta r_c}{\delta r_{c,0}} \right)^2 \quad (\text{B8})$$

<sup>11</sup> Unlike in the estimate in Appendix B1, here the density outside the core need not be constant.

<sup>12</sup> As explained in Footnote 4, in our simulations we introduce a small pressure gradient between the two phases, and thus the flow there remains subsonic. Nevertheless, the large density jump leads to numerical dissipation of comparable strength. We have also performed tests with almost zero pressure gradient and thus supersonic flow across the density jump, and find similar damping time scales of at most a factor 2 shorter. However, for numerical reasons here strong high-frequency noise superimposes the damped pulsations.

and using Eq. (B5), Eq. (B7) can be resolved for  $\delta r_c$ :

$$\frac{1}{(\delta r_c)^3} \frac{d(\delta r_c)^2}{dt} = -\frac{1}{\delta r_{c,0}} \frac{\dot{\bar{E}}_{d,0}}{\bar{E}_{p,0}}. \quad (\text{B9})$$

This can be straightforwardly integrated to

$$\delta r_c = \delta r_{c,0} \left( 1 + \frac{\dot{\bar{E}}_{d,0} t}{2\bar{E}_{p,0}} \right)^{-1} \approx \delta r_{c,0} \frac{2\bar{E}_{p,0}}{\dot{\bar{E}}_{d,0} t}. \quad (\text{B10})$$

With this we have an explicit expression for the time evolution of the pulsation amplitude  $\delta r_c$  of the dense core, which we can apply to get an estimate for the damping time scale of the pulsations. Choosing for instance  $t$  in Eq. (B10) as the time  $\tau_{1/5}$  when the radial perturbations  $\delta r_c$  of the dense core have dropped to  $\delta r_{c,0}/5$  and using the values from Eqs. (B3, B6) for  $\bar{E}_{p,0}$  and  $\dot{\bar{E}}_{d,0}$ , respectively, we obtain  $\tau_{1/5} \approx 12$  ms. The value  $\tau_{1/5} \approx 6$  ms read off from Fig. B1 is shorter, but of the same order of magnitude ( $\sim 10$  ms) as this crude analytic estimate.

Although this treatment is somewhat simplistic, it demonstrates that the compression of matter passing through the phase transition in the microphysical EoS can very efficiently dissipate pulsation energy on a time scale that is consistent with our observations for the family UM of migration models. In contrast, as apparent from Fig. 6 the typical damping times of the models of family US with the simple MUn EoS are much longer, as there the above efficient dissipation mechanism is not at work.

## B3 Non-equilibrium effects and bulk viscosity damping

We now relax the condition of complete equilibration. The phase transition at the core radius  $r_c$  must then be treated by taking into account the slowness of weak interaction processes. Consequently, kaon condensation will proceed off thermodynamic equilibrium. However, the rate of non-equilibrium reactions increases very steeply with the deviation from equilibrium. Therefore, also in this case  $\dot{\bar{E}}_d$  is not significantly smaller than the upper bound obtained in Appendix B2 under the assumption of full equilibration.

In addition, non-equilibrium processes produce entropy in the form of heating up the matter. This effect can be represented by bulk viscosity, corresponding to an additional average dissipation power  $\dot{\bar{E}}_{d,bv}$ .

In the case of a mixed quark-nucleon core, the efficient damping mechanism described in Section B2 does not work, as there exists no single phase interface with a large jump in density. Then the bulk viscosity generated by non-equilibrium, strangeness changing reactions in the quark component,

$$u + d \rightleftharpoons s + u, \quad (\text{B11})$$

becomes the main damping mechanism (see Madsen 1999, and references therein).

If one considers the mini-collapse of an unstable neutron star caused for instance by dynamic migration as in this work rather than a supernova core collapse, the relative post-collapse pulsation amplitude  $|\delta r_s|/r_s$  is typically less than  $6 \times 10^{-2} T/10^9$  K. Therefore, bulk viscosity does not depend

on  $\delta r_s$  and the associated damping exhibits the usual form (Madsen 1999)

$$\delta r_s = \delta r_{s,0} e^{-t/\tau_{\text{bv},q}}, \quad (\text{B12})$$

where  $\tau_{\text{bv},q}$  is the damping time scale. For a strange quark mass of 100 MeV, a Fermi energy of the down quark of 300 MeV, and choosing  $\omega_p = 2\pi/t_p \approx 2 \times 10^4 \text{ s}^{-1}$  one gets, after transforming a formula given in (Madsen 1999),

$$\tau_{\text{bv},q} \approx 0.1 (T_9)^{-2} \left( \frac{r_c}{0.3 r_s} \right)^{-3} \text{ s}. \quad (\text{B13})$$

If the core, however, consists of a kaon condensate, then the bulk viscosity is generated by the non-equilibrium processes



that also change strangeness. For non-superfluid nucleons, this bulk viscosity is independent of temperature and causes a damping of the fundamental radial mode pulsations on a time scale (Chatterjee & Bandyopadhyay 2007)

$$\tau_{\text{bv},k} \approx 100 \left( \frac{r_c}{0.3 r_s} \right)^{-3} \text{ s}, \quad (\text{B15})$$

which is much longer than the corresponding bulk viscosity damping time scale  $\tau_{\text{bv},q}$  in a quark core given in Eq. (B13). Thus here the contribution to damping from bulk viscosity is only a very small part of the total dissipation power, which is dominated by the effects from the first-order phase transition.